Origin of the synergistic effect between TiO_2 crystalline phases in the Ni/TiO_2-catalyzed CO_2 methanation reaction

Messou, Davina; Bernardin, Vincent; Meunier, Frédéric; Ordoño, Marta Borges; Urakawa, Atsushi; Machado, Bruno F.; Collière, Vincent; Philippe, Régis; Serp, Philippe; Le Berre, Carole

DOI
10.1016/j.jcat.2021.04.004

Publication date
2021

Document Version
Accepted author manuscript

Published in
Journal of Catalysis

Origin of the synergistic effect between TiO_2 crystalline phases in the Ni/TiO_2-catalyzed CO_2 methanation reaction

Davina Messou,[a] Vincent Bernardin,[b] Frédéric Meunier,[c] Marta Borges Ordoño,[d] Atsushi Urakawa,[d,e] Bruno F. Machado,[f] Vincent Collière,[a] Régis Philippe,[b] Philippe Serp,[,a] and Carole Le Berre[*,a]*

[a] *LCC-CNRS, INPT, 205 route de Narbonne, 31077 Toulouse Cedex 4, France*

[b] *Catalysis Polymers Processes and Materials (CP2M), Université de Lyon, UMR 5128 CNRS, CPE Lyon, Université Claude Bernard Lyon 1, France*

[c] *Univ. Lyon, Université Claude Bernard Lyon 1, CNRS, IRCELYON, 2 Av. Albert Einstein, 69626 Villeurbanne, France.*

[d] *Institute of Chemical Research of Catalonia (ICIQ), Av. Paisos Catalans 16, 43007 Tarragona, Spain*

[e] *Catalysis Engineering, Department of Chemical Engineering, Delft University of Technology, Van der Maasweg 9, 2629 HZ Delft, The Netherlands*

[f] *Laboratory of Separation and Reaction Engineering - Laboratory of Catalysis and Materials (LSRE-LCM), Chemical Engineering Department, Faculty of Engineering, University of Porto, Rua Dr. Roberto Frias s/n, 4200-465 Porto, Portugal*

Abstract. The catalytic performances of TiO_2-supported Ni catalysts for the methanation of CO_2 have been investigated using different crystalline phases of TiO_2 (rutile and anatase). The catalytic activity of Ni depends appreciably on the nature of the support. The rate for CO_2 hydrogenation decreases in the order of $10Ni/TiO_{2\text{-}rutile}$ >> $10Ni/TiO_{2\text{-}anatase}$. The use of a mixture of catalysts containing 70% $10Ni/TiO_{2\text{-}anatase}$ + 30% $10Ni/TiO_{2\text{-}rutile}$ allows for a significant increase of the reaction rate related to 100% $10Ni/TiO_{2\text{-}rutile}$. Importantly, it has been demonstrated that the two catalysts do not need to be in direct contact for the synergetic effect to occur. DRIFTS *operando* analysis during the methanation reaction shows that adsorbed CO accumulates on $Ni/TiO_{2\text{-}anatase}$ and not on $Ni/TiO_{2\text{-}rutile}$, and that the role of the $Ni/TiO_{2\text{-}rutile}$ is to assist the hydrogenation of this adsorbed CO on the $Ni/TiO_{2\text{-}anatase}$. Increased CO_2 methanation is also observed by adding Ni-free $TiO_{2\text{-}anatase}$ to $10Ni/TiO_{2\text{-}rutile}$, indicating that CO_x hydrogenation can also occur on bare $TiO_{2\text{-}anatase}$ if activated hydrogen can be supplied by another source. H_2-TPD analyses and catalytic tests performed after dilution of the catalysts have shown that hydrogen spillover (mediated by surface or gas-phase species) is at the origin of the synergy observed between the two catalysts for the Sabatier reaction.

Key words: CO_2 methanation, nickel, titania, spillover, rutile, anatase

1. Introduction

The reduction of greenhouse gas emissions, and particularly those of CO_2, which is the main contributor to global warming, is one of the major challenges of the beginning of this century. In addition to reducing the emissions of this gas, two major strategies have been proposed to reduce the amount of CO_2 present in the atmosphere: its capture and storage [1-3] and its chemical transformation [4-6]. The chemical transformation of CO_2 is particularly promising

as increasing amounts of low-cost and relatively pure CO_2 are available from current plants [7]. In this context, CO_2 methanation (Sabatier reaction) is particularly attractive [8-11]. CO_2 can be combined with hydrogen (produced by water electrolysis using renewable electricity) to produce methane (power-to-gas), which can be directly injected into existing natural gas pipelines [12-14]. Therefore, CO_2 methanation makes it possible to combine an environmental benefit with an economic opportunity.

The Sabatier reaction is an exothermic reaction that has been studied using catalytic systems based on Group VIII metals (Ru, Rh, Co, Ni) supported on various oxides (TiO_2, SiO_2, Al_2O_3, CeO_2, ZrO_2) [9, 11]. Nickel remains the metal of choice, due to its selectivity, activity, low price and abundance [15-18]. Haldor Topsøe uses Ni-based catalysts supported on alumina for its own methanation processes (TREMP™ process) [19], and continuous efforts are pursued to develop active, selective and stable Ni-based catalysts able to operate under mild reaction conditions [18, 20-25].

The role of TiO_2 has been recognized in many reactions, as it enhances the catalytic activity due to specific metal-support interactions [26, 27]. TiO_2 exists in three main crystalline forms, *i.e*. anatase ($TiO_{2\text{-}anatase}$), rutile ($TiO_{2\text{-}rutile}$) and brookite. Each phase exhibits different physical and chemical properties, such as thermal stability, density and band gap as well as surface structure [27, 28]. Several works have been conducted to investigate the influence of the support in methanation catalysts: TiO_2 *vs* Al_2O_3 or SiO_2 supports, but also $TiO_{2\text{-}anatase}$ *vs* $TiO_{2\text{-}rutile}$ *vs* $TiO_{2\text{-}P25}$ (a commercial mixture of rutile and anatase phases) [29-34]. On cobalt-based catalysts, the activity of a $Co/TiO_{2\text{-}rutile}$ catalyst is remarkably higher than that of $Co/TiO_{2\text{-}anatase}$; and while CH_4 is selectively produced on $Co/TiO_{2\text{-}rutile}$, CO is the main product on $Co/TiO_{2\text{-}anatase}$. From an *in situ* DRIFT study, it was proposed that the high activity of $Co/TiO_{2\text{-}rutile}$ is related to the formation of strongly adsorbed CO species on this catalyst [29]. On Ru/TiO_2 catalysts, Prairie *et al*. have shown that: i) the high Ru dispersion is believed to contribute to the enhanced activity

for CO_2 methanation, and ii) a synergy exists for mixtures of Ru/$TiO_{2\text{-}anatase}$ and Ru/$TiO_{2\text{-}rutile}$ [30]. From a FTIR study, these authors have evidenced that Ru/$TiO_{2\text{-}anatase}$ is a better catalyst for CO production, while Ru/$TiO_{2\text{-}rutile}$ is more efficient in CO hydrogenation (the rate determining step of methanation). The resulting ranking is as follows: Ru/$TiO_{2\text{-}P25}$ > Ru/TiO_2 (mechanical mixture of anatase and rutile to simulate P25) > Ru/$TiO_{2\text{-}rutile}$ >> Ru/$TiO_{2\text{-}anatase}$. Continuing with ruthenium, Sassoye *et al*. have used different catalyst preparation methods, using different TiO_2 crystalline phases and ratios [31, 32]. Phase mixing was also performed at different stages of the catalyst preparation *i.e*., before RuO_2 deposition, and before or after calcination at 450 °C. These studies have shown that the interaction between the RuO_2 particles and the anatase and rutile TiO_2 phases during the calcination step dictates the performance of the Ru/TiO_2 methanation catalyst. The positive effect of support mixing, correlated with RuO_2 migration and stabilization from $TiO_{2\text{-}anatase}$ over $TiO_{2\text{-}rutile}$, was noticed only in the case where the mixing was done before the calcination step. Regarding nickel-based catalysts, Bao *et al*. have shown that the TOF on Ni/$TiO_{2\text{-}rutile}$ is almost two orders of magnitude higher than that on Ni/$TiO_{2\text{-}anatase}$ for CO_2 methanation, independently of Ni loading and particle size [33]. *In situ* IR and temperature-programmed surface reaction experiments have revealed that $TiO_{2\text{-}rutile}$ significantly enhances the CO dissociation and hydrogenation ability of Ni. To the best of our knowledge, a possible synergy between the anatase and rutile phase of TiO_2 for CO_2 methanation has not yet been demonstrated in the case of nickel, although high catalytic activities have been reported for Ni/$TiO_{2\text{-}P25}$ catalysts [20].

In this study, we have focused our attention on the interaction between nickel and $TiO_{2\text{-}rutile}$ and $TiO_{2\text{-}anatase}$ phases by studying the performances of Ni catalysts supported on $TiO_{2\text{-}rutile}$, $TiO_{2\text{-}anatase}$ and $TiO_{2\text{-}P25}$. We confirmed the better performances of Ni/$TiO_{2\text{-}rutile}$ compared to Ni/$TiO_{2\text{-}anatase}$, and revealed for the first time a synergy between the two phases in the Ni/$TiO_{2\text{-}P25}$ catalyst or in physical mixtures of Ni/$TiO_{2\text{-}rutile}$ and Ni/$TiO_{2\text{-}anatase}$. Catalyst characterizations,

as well as catalytic experiments performed with pure catalysts in two separated and successive fixed-beds, demonstrate that hydrogen spillover is at the origin of the synergistic effect, but also of the different reactivity of $Ni/TiO_{2\text{-}rutile}$ and $Ni/TiO_{2\text{-}anatase}$ catalysts.

2. Methods

Catalyst synthesis. The commercial TiO_2 supports with different structures used are $TiO_{2\text{-}rutile}$ (99.5 %, Janssen Chimica), $TiO_{2\text{-}anatase}$ (99.8 %, Aldrich) and $TiO_{2\text{-}P25}$ (Safic-Alcan). In some experiments, $TiO_{2\text{-}rutile}$ and $TiO_{2\text{-}anatase}$ were physically mixed in the corresponding proportions to those of $TiO_{2\text{-}P25}$.

The Ni catalysts were prepared by using an impregnation method. $Ni(NO_3)_2$, $6H_2O$ (99.9% Strem Chemical) was dissolved in water, where TiO_2 (rutile, anatase or P25) was then added. The mixture was stirred during 4 h. The water was evaporated to obtain the catalyst, which was dried at 120 °C overnight, and calcined under air at 500 °C during 6 h. The desired quantity of $Ni(NO_3)_2$, $6H_2O$ to reach a 10 % w/w was used. According to Inductively Coupled Plasma (ICP) analyses, the amount of nickel deposited on each support is similar. The as-prepared catalysts were denoted as $10Ni/TiO_{2\text{-}rutile}$, $10Ni/TiO_{2\text{-}anatase}$ or $10Ni/TiO_{2\text{-}P25}$ (with 10 representing the Ni percentage on the support).

Catalyst characterization. The structural and textural properties of the catalysts were evaluated using different characterization techniques. The specific surface area, pore volume and pore size distribution of the samples were obtained from the isothermal adsorption/desorption of nitrogen at -196 °C on a Quantachrome autosorb instrument with N_2 automatic injection. The specific surface area was determined from the linear part of the Brunauer-Emmett-Teller (BET) plot. The pore volume was measured on the isotherm at $P/P_0 = 0.97$. The pore size distribution was obtained by BJH treatment applied to the desorption branch of the isotherm. All samples

were pretreated under vacuum at 90 °C for 1 h to remove adsorbed water, then at 250 °C during 10 h for all other physisorbed species.

The amount of surface metal was quantified by chemisorption. Hydrogen was used to determine the dispersion of the metal particles for each catalyst. In a first step, the sample (200 mg) was reduced using hydrogen (30 mL·min^{-1}) at 400 °C (10 °C·min^{-1}) during 4 h. Argon was introduced at the same temperature for 2 h, and then maintained while the reactor cooled to room temperature. At this stage of the analysis, pulses of H_2 were injected on the catalyst, and the amount of residual gas was measured using a TCD detector (Quantachrome autosorb instrument). The metallic dispersion D_{Ni}(%) of the catalysts was calculated from the amount of irreversibly adsorbed hydrogen (HC): D(%) = HC/N_T * 100 (N_T is the total quantity of metallic atom in the sample).

Temperature-Programmed Reduction (TPR) experiments were performed with a Micromeritics chemisorb 2700. Firstly, the catalyst (100 mg) was heated to 200 °C (10 °C·min^{-1}) for 1 h. After the reactor cooled to room temperature, an argon flow (30 mL·min^{-1}) swept the sample for 30 minutes. In a second step, the catalyst was reduced under a gaseous mixture of 10% H_2/Ar (30 mL·min^{-1}) with a heating ramp of 10 °C·min^{-1} to 850 °C. The amount of hydrogen consumed was monitored using a TCD. Peaks of hydrogen consumption were obtained as a function of the temperature.

The distribution, shape, and size of the metal particles were obtained using a JEOL JEM 1011 transmission electron microscope (TEM). The average particle size was determined by measuring at least 100 particles for each sample analyzed and using the following formula: Ni particle size = $\Sigma n_i d_i^3/\Sigma n_i d_i^2$ (d_i = diameter of n_i particles). The high-resolution analyses were conducted on a JEOL JEM 2100F equipped with a field emission gun (FEG) operating at 200 kV with a point resolution of 2.3 Å and a JEOL JEM-ARM200F Cold FEG operating at 200 kV with a point resolution of > 1.9 Å. The crystalline structure of the samples was determined

on a D8 Advance Bruker Diffractometer (XRD) using Cu Kα radiation (λ = 0.15418 nm) as X-ray source. The surface of a sample, to a depth of 1 to 10 nm, was observed by X-ray Photoelectron Spectroscopy (XPS) using a Thermo Scientific K-alpha spectrometer equipped with an aluminum monochromatic source (Al Kα, $h\nu$ = 1486.6 eV). Data were processed using the Thermo Avantage© software.

DRIFTS spectra were collected using a Harrick cell (powder, *ca*. 30 mg) fitted in a Nicolet 8700 FT-IR (MCT detector). Gas-phase CH_4 and CO_2 were quantified after the DRIFTS using a quartz 10-cm pathlength IR gas-cell fitted in a Bruker FT-IR. The CO signal was very low (and not visible for Ni/Rutile) and was not quantified. The band area of adsorbed CO was calculated and compared for three catalysts. The DRIFTS analysis provides quantitative comparison within 10% as long as evolution of the same sample (or same mixture of samples) are compared with each other (hence in each case the optical pathway remains the same). In our case, it is also coherent to compare mechanical mixtures of similar materials, since scattering and absorption coefficient should be similar.

In order to understand the behavior and the synergetic effect between the anatase and rutile phases, space-resolved gas sampling was performed using a fused silica capillary (I.D. = 150 μm) inserted in the catalyst bed that moved along the axial direction; data was collected for each position (9 positions in total) along the catalyst using a mass spectrometer (OmniStar, Pfeiffer Vacuum). The custom-built reactor was made of ¼" quartz tube with an I.D. of 4 mm. For each experiment, 100 mg of catalyst was used with a particle size between 125 and 200 μm.

H_2-TPD-MS (Altamira Instruments AMI-300 device) was used to elucidate the nature of the hydrogen adsorbed species during the desorption step. First, the catalyst (or support) (100 mg) was purged with helium at 120 °C for 1 h in order to clean the surface of the sample. The sample was then reduced *in situ* at 400 °C (10 $^{o}C \cdot min^{-1}$) for 4 h using a 1/4 mixture of He/H_2 and then

cooled to room temperature under the same atmosphere. The sample was then swept with helium at a flow rate of 30 $mL \cdot min^{-1}$ for 1 h to remove physisorbed and/or weakly bound species. TPD was performed by heating the sample from 50 to 700 °C with a heating ramp of 10 $°C \cdot min^{-1}$ in helium and the TPD spectra were recorded.

Catalytic tests. The catalytic tests for the methanation of CO_2 were performed using a continuous-flow stainless steel fixed bed reactor (height = 300 mm, *e.d.* = 9.52 mm, *i.d.* = 7.9 mm) under a total pressure of 6.1 bar. 200 mg of catalyst with a particle size in the 100-200 μm range were mixed with 1800 mg of SiC (Alfa Aesar). Before the catalytic test, the catalyst was reduced *in situ* at 400 °C for 4 h under a 1/4 mixture of N_2/H_2, at atmospheric pressure. Then, experiments were performed at a constant WHSV (Weigh Hourly Space Velocity) of 2750 $NmL_{CO2} \cdot h^{-1} \cdot g^{-1}$. under a $N_2/H_2/CO_2$ gas mixture of 1/4/1 at 340 °C and 6.1 bar. Some tests were also conducted at 260 °C and 6.1 bar, or at 340 °C and 1 bar. Some tests were also performed by dilution of the catalyst in TiO_2 support instead of pure SiC. In typical dilution tests, 200 mg of catalyst were diluted in 1000 mg of TiO_2 support and 800 mg of SiC.

The composition of the reactant/product mixture was analyzed using an on-line gas chromatograph (500 Clarius) equipped with two TCD: one with argon as gas vector to quantify H_2, CH_4, and CO, and another with helium to quantify CO_2. The GC is equipped with two Shincarbon columns (1/8, 2.0 mm, 80/100), and recorded the formation of methane and conversion of H_2 and CO_2 every 8 min.

The different response coefficients determined from the GC calibration allowed us to calculate the molar fractions (X) of the different molecules considered during the methanation reaction, as follows:

$$X_a = \left(\frac{Area\ of\ a\ signal}{Area\ of\ N_2\ signal}\right) \times \frac{1}{k_a}$$

With a = CO_2, CH_4, H_2, CO and k = response coefficient.

The conversion rates of the reagents were then calculated as follows:

$$CO_2\ conversion = \left(1 - \frac{X_{CO_2}}{X_{CO_2}+X_{CH_4}+X_{CO}}\right) \qquad H_2\ conversion = \left(1 - \frac{H_2\ outlet\ flow}{H_2\ inlet\ flow}\right)$$

With $H_2\ outlet\ flow = Dry\ flow\ outlet \times X_{H_2}$

$With\ Dry\ Flow, the\ gas\ flow\ without\ water\ formed\ during\ the\ reaction.$

$$Dry\ flow\ outlet = \left(\frac{CO_2\ inlet\ flow}{X_{CO_2}+X_{CH_4}+X_{CO}}\right) \qquad CH_4\ yield = \left(\frac{CH_4\ outlet\ flow}{CO_2\ inlet\ flow}\right)$$

With $CH_4\ outlet\ flow = Dry\ flow\ outlet \times X_{CH_4}$

$$CO\ yield = CO_2\ conversion - CH_4\ yield$$

$$CH_4\ selectivity = \left(\frac{\%CH_4\ yield}{\%CO_2\ conversion}\right) \qquad CO\ selectivity = \left(\frac{CO\ yield}{CO_2\ conversion}\right)$$

Possible thermodynamic, heat transfers and mass transfer limitations have been checked (see SI 1 and SI 2). When not specified, all the results are due to an intrinsic kinetic effect and thus reflect a catalytic effect. In order to remove any effect of a different level of conversion between experiments, the quantitative comparison of catalysts has been achieved through a robust kinetic comparison on the basis of estimated inlet CO_2 consumption rates ($r^{i}_{co_2}$) at the reactor inlet. This goal was achieved thanks to a non-isothermal and non-isobaric unidimensional pseudo-homogeneous plug-flow reactor model combined with the regression of a limited set of kinetic parameters of the kinetic model from Champon *et al.*[36] More details on this approach are available in the SI 3. The CO_2 consumption rates at the inlet ($r^{i}_{CO_2}$), can then be used to calculate corresponding TOF_i at the reactor inlet. These TOF_i, which refer to the number of reacted molecules per surface active Ni per unit of time at the reactor inlet, have been calculated

considering dispersion data (TEM mean particle size after testing) obtained from a universal mathematical relation [35].

Catalyst stability was evaluated considering a deactivation parameter (DP) based on the evolution of the inlet reaction rate of CO_2 hydrogenation with time on stream (TOS) defined as follows:

$$DP = \frac{\left(r^{i}_{CO_2}\right)_{TOS=20h} - \left(r^{i}_{CO_2}\right)_{TOS=1h}}{\left(r^{i}_{CO_2}\right)_{TOS=1h}}$$

Because of possible differences in catalyst activity and active specie dispersion, a Turn Over Number (TON, expressed in $mol_{CO2\ converted}$ per $mol_{Ni\ surf.}$) is always given simultaneously to reflect the corresponding work of the catalyst.

3. Results

3.1. Catalyst characterization

The specific surface area, pore volume, average pore diameter, Ni loading (ICP), Ni mean particle size and dispersion of the investigated samples are shown in Table 1. The BET area of commercial TiO_2 supports follows the sequence $TiO_{2\text{-}P25}$ (57 $m^2\ g^{-1}$) > $TiO_{2\text{-}anatase}$ (10 $m^2\ g^{-1}$) > $TiO_{2\text{-}rutile}$ (4 $m^2\ g^{-1}$). As already reported for similar catalysts [20], the addition of nickel by impregnation induces a decrease of the specific surface area for the $TiO_{2\text{-}P25}$-based catalyst. Figure 1 shows the H_2-TPR profiles of the calcined Ni/TiO_2 samples, which correspond to the reduction of NiO. The catalysts can be classified according to their reducibility in the following order: $10Ni/TiO_{2\text{-}rutile}$ ~ $10Ni/TiO_{2\text{-}anatase}$ > $10Ni/TiO_{2\text{-}P25}$. For $10Ni/TiO_{2\text{-}rutile}$ and $10Ni/TiO_{2\text{-}anatase}$ catalysts, the H_2-TPR profile presents a main reduction peak at 420 and 440 °C,

respectively. An easier reduction of NiO to Ni^0 for $Ni/TiO_{2\text{-}rutile}$ compared to $Ni/TiO_{2\text{-}anatase}$ has been previously reported [37]. The $10Ni/TiO_{2\text{-}P25}$ catalyst profile is relatively broad (stepwise Ni reduction) and the lower reducibility suggests a stronger interaction between Ni and the support, arising presumably from a smaller Ni particle size. Previous H_2-TPR experiments on $Ni/TiO_{2\text{-}anatase}$ and $Ni/TiO_{2\text{-}rutile}$ have also proposed a stepwise reduction of Ni [33]. Finally, if the discussion on the TPR profiles of Ni/TiO_2 catalysts are generally limited to the reduction of NiO species presenting different type of interaction with the support, some works [38, 39] also reported that the NiO phase reduction can be accompanied by a partial reduction of Ti^{4+} to Ti^{3+}, resulting in the formation of O_v- Ti^{3+} site (where O_v denotes oxygen vacancy). It is not possible to exclude the occurrence of such a phenomenon in our case.

The Ni particle size was obtained from both XRD and TEM analyses (Table 1). The TEM and XRD analyses confirmed a smaller Ni particle size on the $TiO_{2\text{-}P25}$ support.

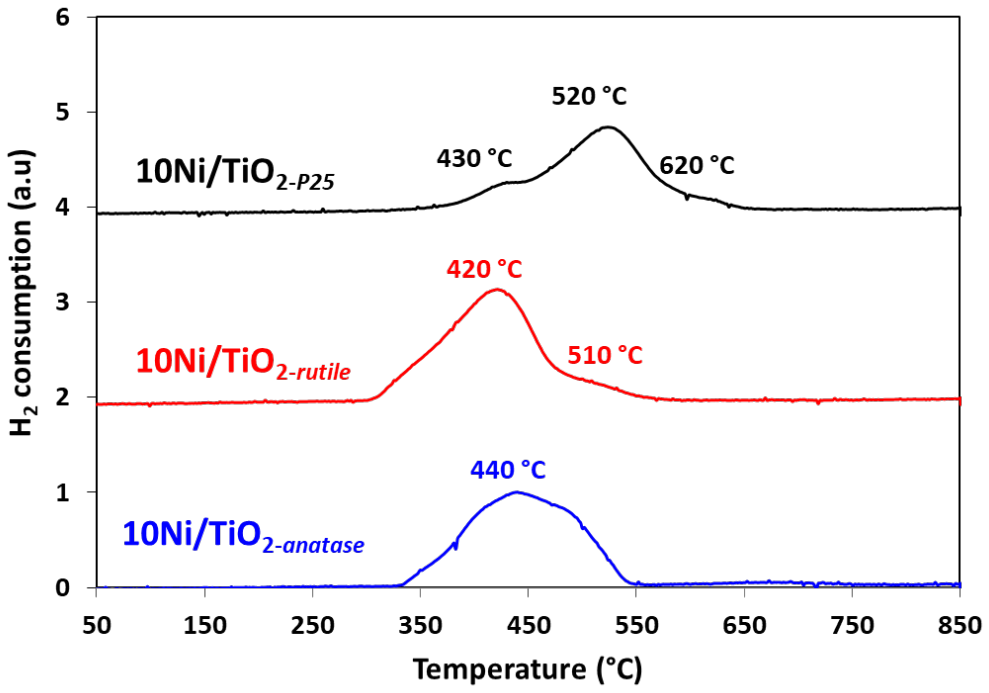

Figure 1. H_2-TPR profiles for the $10Ni/TiO_{2\text{-}anatase}$, $10Ni/TiO_{2\text{-}rutile}$ and $10Ni/TiO_{2\text{-}P25}$ catalysts.

In XRD, the characteristic NiO peak is identified at 2θ = 43.55° (Figure 2). Although it has been shown that the anatase-rutile transformation of the TiO_2 support is facilitated by the metallic ions formed during the reduction [40]; such phenomenon was not significant in the present study. The amount of anatase phase in $TiO_{2\text{-}P25}$ (78 %) was determined from the equation proposed by Spurr and Myer [41]:

$$\%\ anatase = (1 + 1.26 * (\frac{Ir}{Ia}))^{-1}$$

where I_a (2θ = 25.4°) and I_r (2θ = 27.6°) are the XRD peak intensities of the anatase and rutile crystal components, respectively.

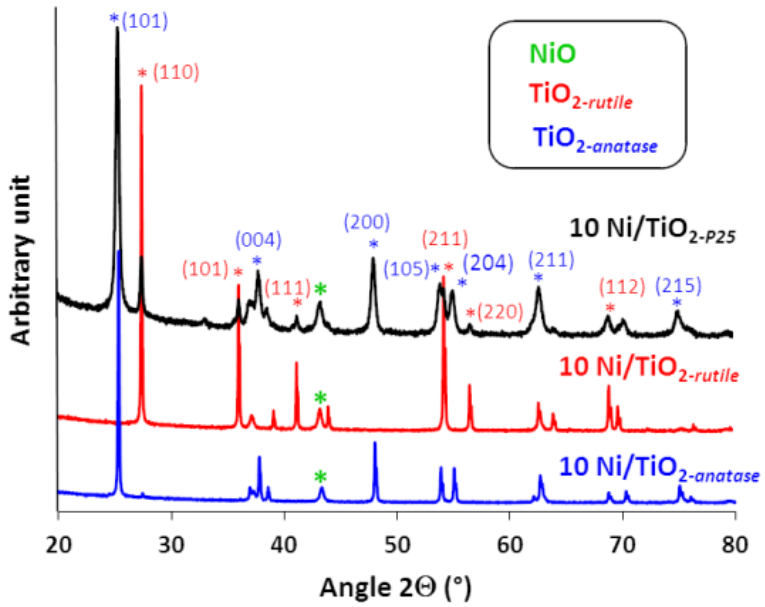

Figure 2. XRD diffractograms for the 10Ni/$TiO_{2\text{-}anatase}$, 10Ni/$TiO_{2\text{-}rutile}$ and 10Ni/$TiO_{2\text{-}P25}$ catalysts.

The images obtained by conventional TEM (Figure 3a-c) allowed us to compare the morphology of the catalysts and to determine the corresponding Ni particle size distribution

(Figure S1). STEM-HAADF images (Figure 3d-f) and EDX mapping (Figure 3g-i) demonstrate the presence of Ni particles on the three catalysts. The Ni particles are larger on $TiO_{2\text{-}rutile}$ and $TiO_{2\text{-}anatase}$ supports. Nickel is relatively well dispersed, especially on the $10Ni/TiO_{2\text{-}P25}$ catalyst, presumably due to the significantly higher surface area of this support. Although TEM studies have revealed that Ni particles show a non-wetting morphology when grown on $TiO_{2\text{-}anatase}$ and a wetting morphology when grown on the rutile (101) surface [42], in our case HRTEM observations (Figure S2) were not conclusive regarding such a phenomenon, even if it appears that the Ni particles on $TiO_{2\text{-}rutile}$ were more facetted than the ones on $TiO_{2\text{-}anatase}$ (Figures 3a,b and Figure S3).

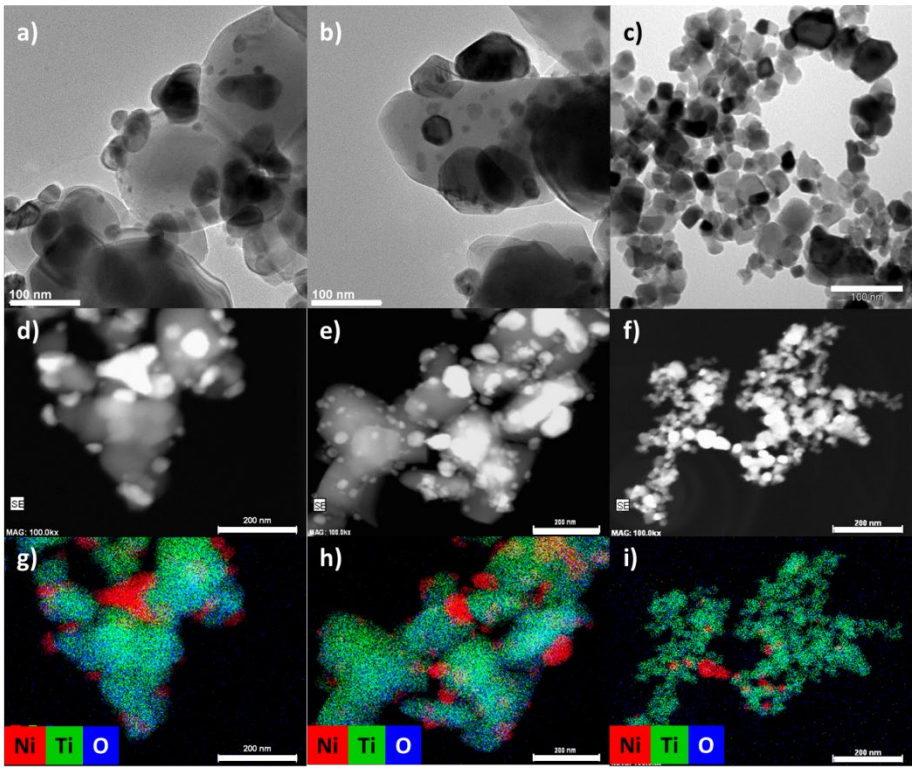

Figure 3. TEM images of a) $10Ni/TiO_{2\text{-}anatase}$, b) $10Ni/TiO_{2\text{-}rutile}$ and c) $10Ni/TiO_{2\text{-}P25}$; STEM-HAADF images of d) $10Ni/TiO_{2\text{-}anatase}$, e) $10Ni/TiO_{2\text{-}rutile}$ and f) $10Ni/TiO_{2\text{-}P25}$; and EDX mapping of g) $10Ni/TiO_{2\text{-}anatase}$, h) $10Ni/TiO_{2\text{-}rutile}$ and i) $10Ni/TiO_{2\text{-}P25}$. Scale bar (a-c): 100nm; (d-i): 200 nm.

The dispersion values of the catalysts obtained by hydrogen chemisorption are very low (0.1-1%). Similar results have already been reported, and have been rationalized by the fact that hydrogen adsorption on Ni/TiO_2 is an activated process [43]. In all cases, the dispersion values calculated from the average particle sizes determined by TEM differ from the chemisorption experimental values. However, the trends remain the same. The H_2 adsorption capacity on the various catalysts decreases according to the following order: $TiO_{2\text{-}P25} > TiO_{2\text{-}rutile} \approx TiO_{2\text{-}anatase}$. Since CO adsorption at low temperature (< 200 °C) may result in $[Ni(CO)_4]$ formation [44], Ni corrosion and Ni deposition in the setup and lines, CO chemisorption was not performed.

XPS analyses were performed just after reducing the samples at 400 °C. The deconvolutions of the Ni $2p_{3/2}$ region of the three catalysts are presented on Figure 4. The chemical states of Ni considered are the following [45-48]:

- Ni^0 particles: 1 peak at 852.6 eV and 2 satellite peaks (856.3 eV and 858.7 eV)
- NiO: 1 peak at 853.7 eV and 4 satellite peaks (855.4 eV, 860.9 eV, 864.0 eV, and 866.3 eV)
- $Ni(OH)_2$: 1 peak at 855.6 eV and 5 satellite peaks (855.7 eV, 857.7 eV, 860.5 eV, 861.5 eV and 866.5 eV).

Nickel is present as Ni^0, NiO and $Ni(OH)_2$ on the three catalysts. The superposition of the bands does not show any significant differences between the different catalysts at the level of the binding energies. Table 2 groups relevant results obtained after deconvolution of the XPS spectra. The atomic percentage and binding energies associated with all the corresponding peaks are given in Table S8. The relative atomic percentage of Ni^0 follows the order $10Ni/TiO_{2\text{-}anatase} > 10Ni/TiO_{2\text{-}rutile} > 10Ni/TiO_{2\text{-}P25}$. The lower amount of Ni^0 on $10Ni/TiO_{2\text{-}P25}$ is in accordance with the TPR results, and should be due to the smaller particle size measured for this catalyst. Indeed, small Ni^0 particles interact strongly with the support, and react with oxygen at a faster rate than with large particles [49].

Table 1. Specific surface area, pore volume, average pore diameter, Ni loading (ICP), Ni mean particle size and dispersion of the investigated samples.

Sample	BET surface area (m^2 g^{-1})	Pore volume (cm^3 g^{-1})	Average pore diameter (nm)	%Ni	Ni particle size (nm)[a]	Ni particle size (nm)[b]	Ni particle size (nm)[c]	D_{Ni} (%)[d]
$TiO_{2\text{-}anatase}$	10	0.12	15	-	-	-	-	-
$TiO_{2\text{-}rutile}$	4	0.05	15	-	-	-	-	-
$TiO_{2\text{-}P25}$	57	0.31	17	-	-	-	-	-
$10Ni/TiO_{2\text{-}anatase}$	10	0.14	17	11.0	31	24	27	4.4
$10Ni/TiO_{2\text{-}rutile}$	4	0.05	16	10.1	33	27	29	4.1
$10Ni/TiO_{2\text{-}P25}$	47	0.37	15	10.1	22	17	20	6.1

[a] The Ni crystal size after reduction, from TEM.
[b] The Ni crystal size after reduction, from XRD.
[c] The Ni crystal size after catalysis (340°C, time-on-stream (TOS) = 25 h), from TEM.
[d] Dispersion of Ni, calculated from the average particle sizes determined by TEM.

Regarding the difference between 10Ni/$TiO_{2\text{-}anatase}$ (36 % Ni^0) and 10Ni/$TiO_{2\text{-}rutile}$ (25.5 % Ni^0), it might be related to the different Ni/Ti surface atomic ratios in these samples. The 10Ni/$TiO_{2\text{-}rutile}$ catalyst shows a significantly higher ratio (0.81) than 10Ni/$TiO_{2\text{-}anatase}$ (0.31), which should result from the lower surface area of the $TiO_{2\text{-}rutile}$ support. Another explanation for the higher Ni/Ti surface atomic ratio observed on 10Ni/$TiO_{2\text{-}rutile}$ could arise from the fact that Ni particles on $TiO_{2\text{-}anatase}$ are wrapped by a thin TiO_x overlayer [33, 50].

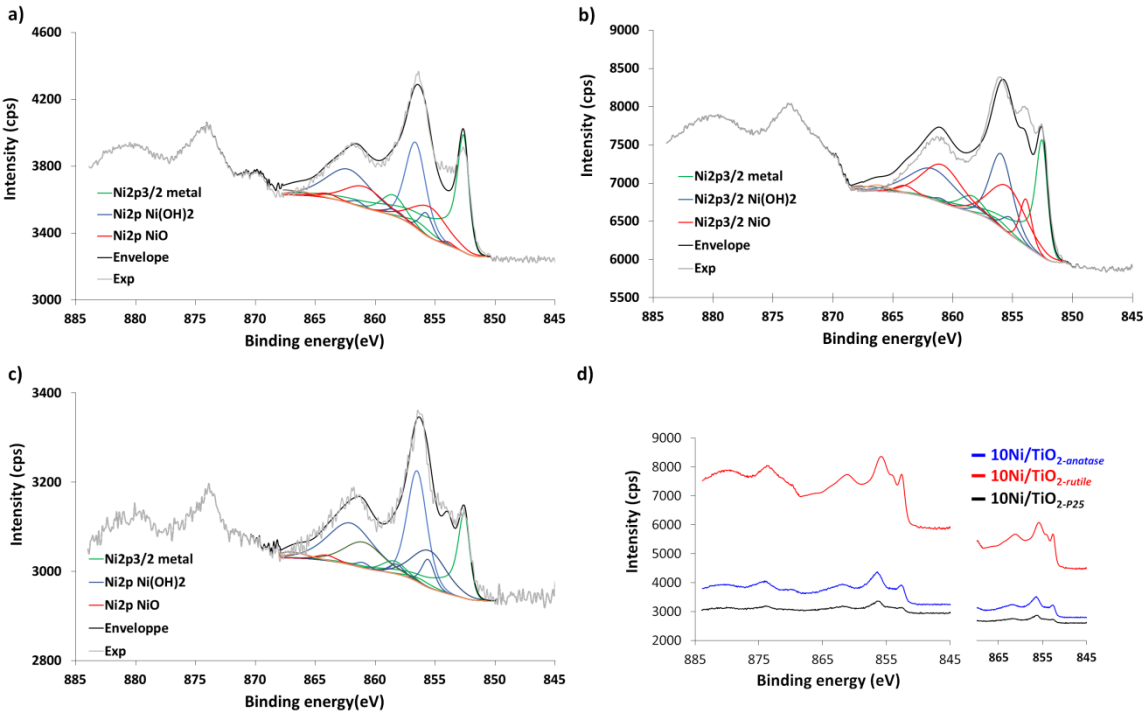

Figure 4. Deconvolutions of Ni $2p_{3/2}$ peak of the catalysts, after *ex-situ* reduction under H_2 at 500 °C a) 10Ni/$TiO_{2\text{-}anatase}$, b) 10Ni/$TiO_{2\text{-}rutile}$, and c) 10Ni/$TiO_{2\text{-}P25}$. d) Superposition of the Ni $2p_{3/2}$ bands of the three samples.

However, our HRTEM observations and STEM-EDX analyses (Figures S4), as well as the catalytic results (see below) do not support this possibility on any of the three supports. This is understandable if we consider that for Ni/TiO_2 catalysts, strong metal support interactions are

significant when a high calcination temperature is used, typically around 800 °C [51, 52]. The low Ni/Ti surface atomic ratio measured for 10Ni/$TiO_{2\text{-}P25}$ should be related to the much higher specific surface area of this catalyst. No significant changes in the Ni^0 binding energy were noticed for the three catalysts, precluding significant differences in charge transfer between these samples, which could affect selectivity in the Sabatier reaction [53, 54]. This is expected if we consider the large Ni particle size; but we cannot exclude that some differences exist in the interfacial region between the metal and the support. Titanium is in the Ti^{4+} form, and the Ti^{3+} form characteristic of reduced TiO_2 [55] was not detected (Figure S5) under these conditions. From HRTEM observations, STEM-EDX analyses (Figures S4) and these XPS data, we can thus exclude the mobility of TiO_{2-x} over the nickel surface.

Table 2. Atomic relative percentage of Ni species, Ni^0 and Ti binding energy and Ni/Ti at. ratios of the catalysts determined by XPS analyses after *ex situ* reduction under H_2 at 400 °C.

Catalyst	Ni^0 (%)	$Ni(OH)_2$ (%)	NiO (%)	Ni^0 B.E. (eV)	Ti B.E. (eV)	Ni/Ti
10Ni/$TiO_{2\text{-}anatase}$	36.0	42.0	22.0	852.6	459.1	0.31
10Ni/$TiO_{2\text{-}rutile}$	25.5	35.6	38.9	852.5	459.2	0.81
10Ni/$TiO_{2\text{-}P25}$	19.7	50.6	29.6	852.6	459.3	0.14

Based on the above analyses, we can conclude that the main difference between the three catalysts arise mainly from the higher BET surface area of $TiO_{2\text{-}P25}$, which allows a better nickel dispersion on that support. The smaller Ni particles present on $TiO_{2\text{-}P25}$ are more difficult to reduce than those supported on $TiO_{2\text{-}anatase}$ or $TiO_{2\text{-}rutile}$. The higher dispersion of Ni on 10Ni/$TiO_{2\text{-}P25}$ should result in a higher catalytic activity for CO_2 methanation, as demonstrated by Wei *et al*. [20].

3.2. Evaluation of the catalytic behavior

The catalytic performances of the obtained Ni/TiO_2 catalysts towards the reaction of CO_2 methanation were studied under different configurations: i) pure catalysts in single fixed-bed reactor configuration; ii) mixture of catalysts in single fixed-bed reactor configuration, and iii) pure catalysts in two separated and successive fixed-beds. Reproducibility tests were regularly performed on the 10Ni/$TiO_{2\text{-}P25}$ catalyst, showing experiment error in the range ± 5%.

Pure catalysts in single fixed-bed reactor configuration. Figure 5 shows the CO_2 consumption rates at the inlet of the reactor ($r^{i}_{co_2}$) and CH_4 selectivity of 10Ni/$TiO_{2\text{-}anatase}$, 10Ni/$TiO_{2\text{-}P25}$, and 10Ni/$TiO_{2\text{-}rutile}$ at 260 °C. Table 3 summarizes the values of CO_2 conversion, CH_4 selectivity, CO_2 consumption rate and initial TOF at 260 and 340 °C. At 260 °C, the conversion values were all below 10%, far from the thermodynamic equilibrium composition. Thus, any thermodynamic limitation can be excluded at 260°C (see SI 1-2 for further details). The reaction rate at the inlet of the reactor $r^{i}_{co_2}$ of the three catalysts follows the order: 10Ni/$TiO_{2\text{-}P25}$ > 10Ni/$TiO_{2\text{-}rutile}$ >> 10Ni/$TiO_{2\text{-}anatase}$ ($k_{CO2meth}$ kinetics constants are given in SI.2, Table S7). These results confirm the findings of Bao *et al*. for Ni/TiO_2 catalysts; *i.e.* Ni/$TiO_{2\text{-}rutile}$ is much more active than Ni/$TiO_{2\text{-}anatase}$ for CO_2 methanation [33]. Since the 10Ni/$TiO_{2\text{-}P25}$ catalyst presents a smaller mean Ni particle size compared to 10Ni/$TiO_{2\text{-}rutile}$ and 10Ni/$TiO_{2\text{-}anatase}$ catalysts (Table 1), the TOF_i led to the following order 10Ni/$TiO_{2\text{-}rutile}$ ≈ 10Ni/$TiO_{2\text{-}P25}$ >> 10Ni/$TiO_{2\text{-}anatase}$. Additionally, as the Ni particle size is significantly smaller on $TiO_{2\text{-}P25}$ than on $TiO_{2\text{-}rutile}$, no obvious structure sensitivity is apparent in the particle size range investigated. Considering that: i) the Ni particle size is similar on 10Ni/$TiO_{2\text{-}anatase}$ and 10Ni/$TiO_{2\text{-}rutile}$ catalysts, ii) no TiO_x overlayer is present on these particles, and iii) the nature of the metal/support interaction is not significantly different for these catalysts (except maybe at the interface), it is reasonable to propose that all catalysts should contain mainly interfacial actives sites, *i.e*. those located at the gas/particle/support interface [56].

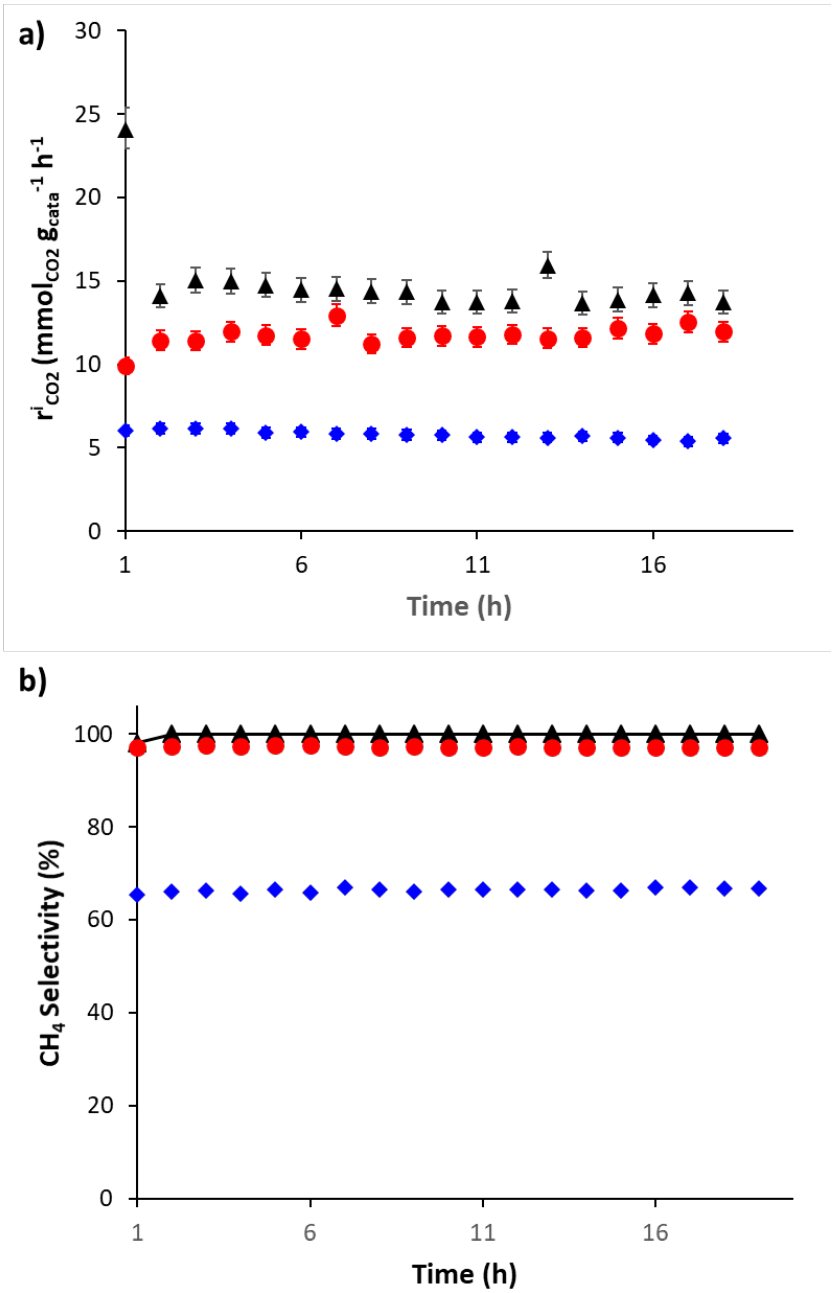

Figure 5. Comparison of: a) CO_2 consumption rates at the inlet of the reactor; and b) CH_4 selectivity of 10Ni catalyst on 10Ni/$TiO_{2\text{-}anatase}$ (blue diamonds), 10Ni/$TiO_{2\text{-}rutile}$ (red circles) and 10Ni/$TiO_{2\text{-}P25}$ (black triangles) at 260 °C.

Table 3. CO_2 conversion, CH_4 selectivity, CO_2 consumption rate and initial TOF (TOF_i) of Ni catalysts on different supports obtained at 260 °C and 340 °C.

Catalyst	CO_2 conv. (%)[a]	CH_4 selec.(%)[a]	$\mathbf{r^i_{co_2}}$ ($mmol_{CO2}\ g_{cat}^{-1}\ h^{-1}$)	TOF_i (h^{-1})
10Ni/$TiO_{2\text{-}anatase}$	4.5 (42.6)	66.4 (79)	5.8	71
10Ni/$TiO_{2\text{-}rutile}$	8.8 (78.4)	99.5 (98.3)	11.7	166
10Ni/$TiO_{2\text{-}P25}$	11.0 (95.6)	99.9 (99.5)	15.1	146

[a] The values between brackets are the value obtained at 340 °C.

As far as selectivity is concerned, it follows the order: 10Ni/$TiO_{2\text{-}P25}$ ≈ 10Ni/$TiO_{2\text{-}rutile}$ > 10Ni/$TiO_{2\text{-}anatase}$. In the case of 10Ni/$TiO_{2\text{-}anatase}$, higher amounts of CO are produced. It has also been shown that the binding strengths of key reaction intermediates at the metal/oxide interface determine the reaction pathways and selectivity in CO_2 hydrogenation reactions [57, 58]. The presence of Ni single atoms or very small nanoparticles or clusters that bind CO too weakly, could also facilitate an easy desorption [54, 59, 60].

The stability of the catalyst is also an important property for CO_2 methanation because of possible Ni sintering and coke deposition under the exothermic reaction conditions, which can lead to fast deactivation. The catalyst stability was investigated for the three catalysts using deactivation parameter (DP) representing the relative loss in reaction rate at the inlet of the reactor and a corresponding TON. These evaluations were done at 260 °C and 340 °C under a constant GHSV of 16500 NmL/h/g_{cata} for a time on stream of 20 h. For the experiments at 260 °C (Figure S6), no detectable deactivation occurs during 20 h for 10Ni/$TiO_{2\text{-}rutile}$ and 10Ni/$TiO_{2\text{-}P25}$ and a slight one for 10Ni/$TiO_{2\text{-}anatase}$ with a DP around 7 %. Final TON values of 1340, 2750 and 2214 are reached for a TOS of 20 h at 260 °C for 10Ni/$TiO_{2\text{-}anatase}$, 10Ni/$TiO_{2\text{-}rutile}$ and 10Ni/$TiO_{2\text{-}P25}$ respectively. The same experiments run at 340°C (Figure S6) indicate again that no detectable deactivation was observed for 10Ni/$TiO_{2\text{-}rutile}$ and 10Ni/$TiO_{2\text{-}P25}$ and a pronounced one is observed for 10Ni/$_{anatase}$ (DP = -62%). Nonetheless, the high conversion level encountered with 10Ni/$TiO_{2\text{-}P25}$ at this temperature is too close to the thermodynamic equilibrium to draw any robust conclusion on the catalyst stability at this temperature for this catalyst. One can just reasonably expect that it is due to its similarity with the rutile catalyst.

The final TON values reached during these experiments are logically higher than the former ones and are of 12 710, 27 250 and 22 370 for 10Ni/$TiO_{2\text{-}anatase}$, 10Ni/$TiO_{2\text{-}rutile}$ and 10Ni/$TiO_{2\text{-}P25}$ respectively. Deactivation of Ni/TiO_2 catalysts during CO_2 methanation has been ascribed either to coke formation through either CH_4 decomposition, or *via* CO disproportionation [24],

or to nickel oxidation [61]. It is interesting to notice that this deactivation is more likely on the catalyst prepared on the anatase phase, which also produces more CO available for disproportionation.

Mixtures of catalysts in single fixed-bed reactor configuration. In order to obtain more information on the influence of the TiO_2 phase on the catalytic performances, calcined 10Ni/$TiO_{2\text{-}anatase}$ and 10Ni/$TiO_{2\text{-}rutile}$ catalysts were physically mixed at different weight ratio. Table 4 shows the CO_2 conversion, CH_4 selectivity, CO_2 consumption rate and inlet TOF_i of these catalyst mixtures. Figure S7 shows the evolution with ToS of CO_2 consumption rate and CH_4 selectivity. The use of 10Ni/$TiO_{2\text{-}anatase}$ and 10Ni/$TiO_{2\text{-}rutile}$ catalyst mixtures (presenting similar particle sizes) improves the CO_2 consumption rate, and a synergistic effect is evidenced ($k_{CO2meth}$ kinetics constants are given in SI.2, Table S7). Interestingly, the synergistic effect was noticed even if the catalysts were mixed after the calcination step, which differs from the work of Sassoye *et al*. [31,32]. Figure 6 shows the inlet CO_2 consumption rate and the corresponding TOF_i for the mixed series from pure 10Ni/$TiO_{2\text{-}anatase}$ to pure 10Ni/$TiO_{2\text{-}rutile}$ catalyst, as a function of the anatase content in the supports. A synergy is clearly observed for a % of 10Ni/$TiO_{2\text{-}anatase}$ between 40 and 80%, as the catalyst mixtures are more active than the corresponding calculated weighted rates based on single-phase rates. The highest TOF_i was obtained for a ratio 70/30, close to the 72/28 ratio of $TiO_{2\text{-}P25}$. It is worth noting that the TOF_i of the 70/30 mixture (211 h^{-1}, Table 4) is markedly higher than that of 10Ni/$TiO_{2\text{-}P25}$ (146 h^{-1}).

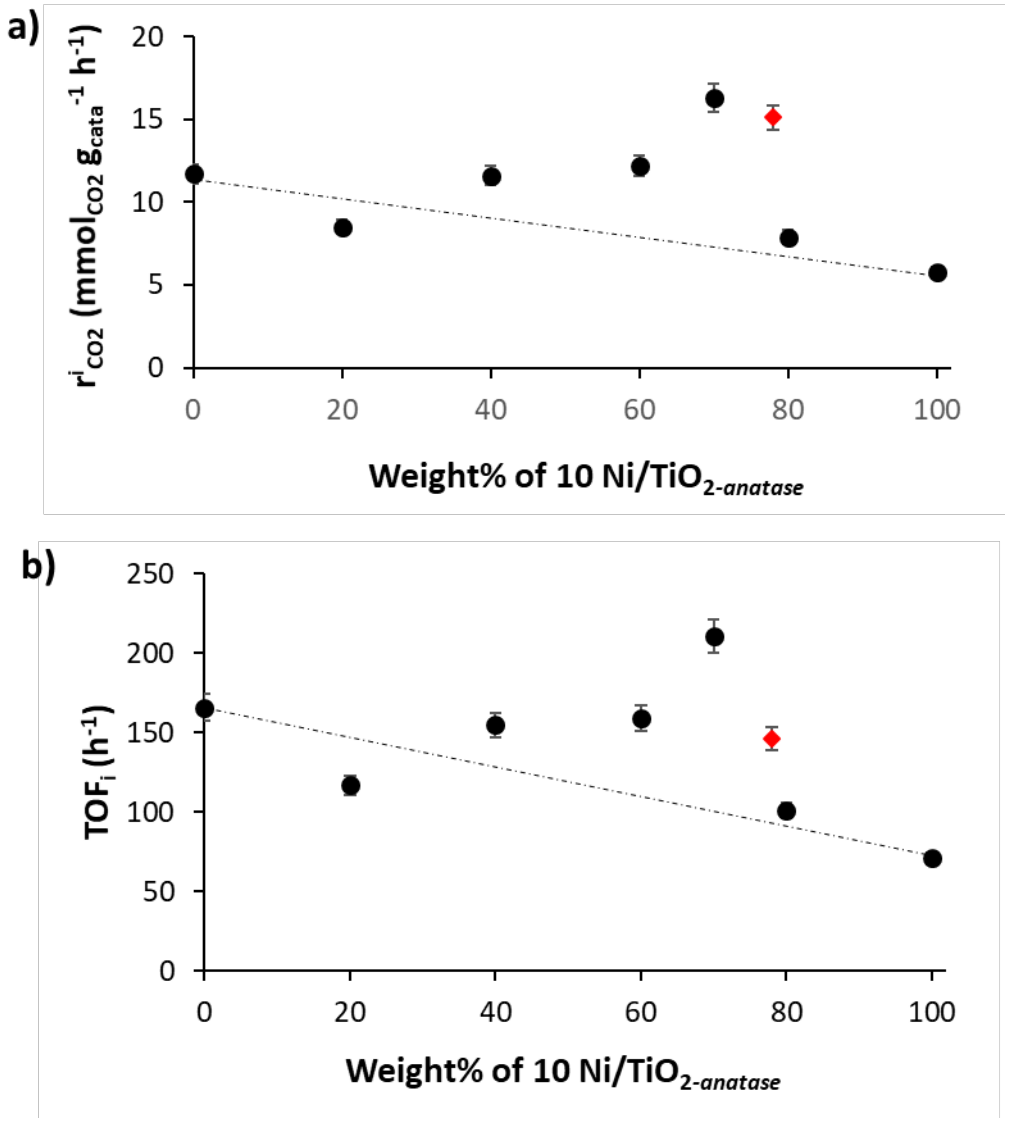

Figure 6. a) CO_2 consumption rate at the inlet of the reactor; and b) TOF_i at 260 °C for the mixed series from pure 10Ni/$TiO_{2\text{-}anatase}$ to pure 10Ni/$TiO_{2\text{-}rutile}$ catalyst, as a function of the anatase content. The full lines indicate the calculated weighted average of 10Ni/$TiO_{2\text{-}anatase}$ and 10Ni/$TiO_{2\text{-}rutile}$ individual performances. The red diamond corresponds to the 10Ni/$TiO_{2\text{-}P25}$ catalyst.

Table 4. CO_2 conversion, CH_4 selectivity, CO_2 consumption rate (sum of methanation reaction rate and RWGS reaction rate) at the inlet of the reactor, initial TOF, and specific activity of 10Ni/$TiO_{2\text{-}anatase}$ + 10Ni/$TiO_{2\text{-}rutile}$ at different ratio and 260 °C (average values after 20 h).

10Ni/$TiO_{2\text{-}anatase}$/10Ni/$TiO_{2\text{-}rutile}$ (weight %)	**CO_2 conv. (%)**	**CH_4 selec. (%)**	**$r^i_{co_2}$ ($mmol_{CO_2}\ g_{cat}^{-1}\ h^{-1}$)**	**TOF_i (h^{-1})**
100/0	4.5	66.4	5.8	71
80/20	6.1	87.9	7.9	101
70/30	11.9	97.8	16.3	211
60/40	9.1	92.7	12.2	159
40/60	8.7	94.7	11.6	155
20/80	6.5	94.7	8.5	117
0/100	8.8	97.2	11.7	166

Pure catalysts in two separated and successive fixed-beds. We performed a series of experiments with two successive beds of 10Ni/$TiO_{2\text{-}anatase}$ and 10Ni/$TiO_{2\text{-}rutile}$ (Figure S8 shows the two reactor configurations with the two separated beds). In the first configuration (**C1**), the gas flow passes first through a bed of 10Ni/$TiO_{2\text{-}rutile}$, and then through a separate bed of 10Ni/$TiO_{2\text{-}anatase}$. In the second configuration (**C2**), the gas flow passes first through a bed of 10Ni/$TiO_{2\text{-}anatase}$, and then through a separated bed of 10Ni/$TiO_{2\text{-}rutile}$. It is important to note that in these two configurations the two beds are not in physical contact since they are separated using quartz wool. The results of this series of experiments are summarized in Table 5.

Table 5. CO_2 conversion and CH_4 selectivity of two successive beds of 10Ni/$TiO_{2\text{-rutile}}$ (20%) and 10Ni/$TiO_{2\text{-}anatase}$ (80%) and *vice versa* at 260 °C. Conversion and selectivity reported here are average values for 20 h of TOS.

Configuration	CO_2 conv. (%)	CH_4 selec. (%)
C1 *first 10Ni/$TiO_{2\text{-}rutile}$ then 10Ni/$TiO_{2\text{-}anatase}$*	11 (5.6)[a]	84.4 (78.6)[a]
C2 *first 10Ni/$TiO_{2\text{-}anatase}$ then 10Ni/$TiO_{2\text{-}rutile}$*	3.5 (5.4)[a]	97.9 (77.1)[a]

[a] Expected values (without the synergy) obtained by the simulation of the two successive beds using regressed kinetic parameters of pure 10Ni/TiO_2-rutile and pure 10Ni/TiO_2-anatase are given between brackets.

This series of experiments is important since it clearly demonstrated that a physical contact between the two catalysts is not necessary to obtain the synergistic effect in the case of the configuration **C1**. Our results contrast significantly with previous studies showing an influence of the TiO_2 crystallographic phase on CO_2 methanation, since: i) from XPS analyses, activity does not seem to be linked to a different electronic interaction between Ni and TiO_2 as previously discussed [33], except maybe at the interface where should be located the active

sites; and ii) the hypothesis of metal migration [31] is excluded from this latter experiment series.

3.3. Space resolved-gas-sampling analyses.

The following conditions were used for space-resolved gas sampling during CO_2 methanation: P_{total} = 1 bar, T = 340 °C; $CO_2/H_2/He$ = 1/4/10; WHSV = 1200 NmL_{CO2} h^{-1} g^{-1}.Under these conditions, CO_2, CH_4, and CO were quantified using an FTIR spectrometer to follow the gas phase composition under different reactor configurations: i) 10Ni/$TiO_{2\text{-}anatase}$; ii) 10Ni/$TiO_{2\text{-}rutile}$; iii) 10Ni/$TiO_{2\text{-}anatase}$ (80%) +10Ni/$TiO_{2\text{-}rutile}$ (20%) catalyst mixture; iv) two beds configuration - first 10Ni/$TiO_{2\text{-}anatase}$ (80%) then 10Ni/$TiO_{2\text{-}rutile}$ (20%); and v) two beds configuration - first 10Ni/$TiO_{2\text{-}rutile}$ (20%) then 10Ni/$TiO_{2\text{-}anatase}$ (80%). The catalytic results (conversion and selectivity) obtained at atmospheric pressure in these experiments as well as in the methanation reactor are presented on Table S9 and Table S10, respectively. The space-resolved gas sampling was performed using a capillary inserted in the catalyst bed (Figure S9) that moved along the axial direction; data were collected for each position along the catalyst using MS. The quantitative results obtained are summarized on Figure 7. This series of experiments shows that 10Ni/$TiO_{2\text{-}rutile}$ promotes the formation of CH_4 (Figure 7b), while 10Ni/$TiO_{2\text{-}anatase}$ promotes the RWGS reaction with formation of CO, together with CH_4 (Figure 7a). When the 2-bed configuration is used, it is observed that: i) in the configuration 10Ni/$TiO_{2\text{-}rutile}$ first, CO_2 methanation occurs first, and then on 10Ni/$TiO_{2\text{-}anatase}$ RWGS comparably more accelerated; and ii) in the configuration 10Ni/$TiO_{2\text{-}anatase}$ first, first CO_2 methanation and RWGS take place, the evolved CO on Ni/$TiO_{2\text{-}anatase}$ does not further react on the Ni/$TiO_{2\text{-}rutile}$ catalyst that only produces more CH_4 and water. Due to the rather low activity at the atmospheric pressure of this space-resolved gas sampling study, the differences between the two sequential-bed configurations are not large. Nevertheless, the selectivity trends defined by the support

structure and also the advantage of the close vicinity of the anatase TiO_2 and rutile TiO_2 supported Ni catalysts on methanation activity is evident (Figure 7c vs. Figures 7d and 7e).

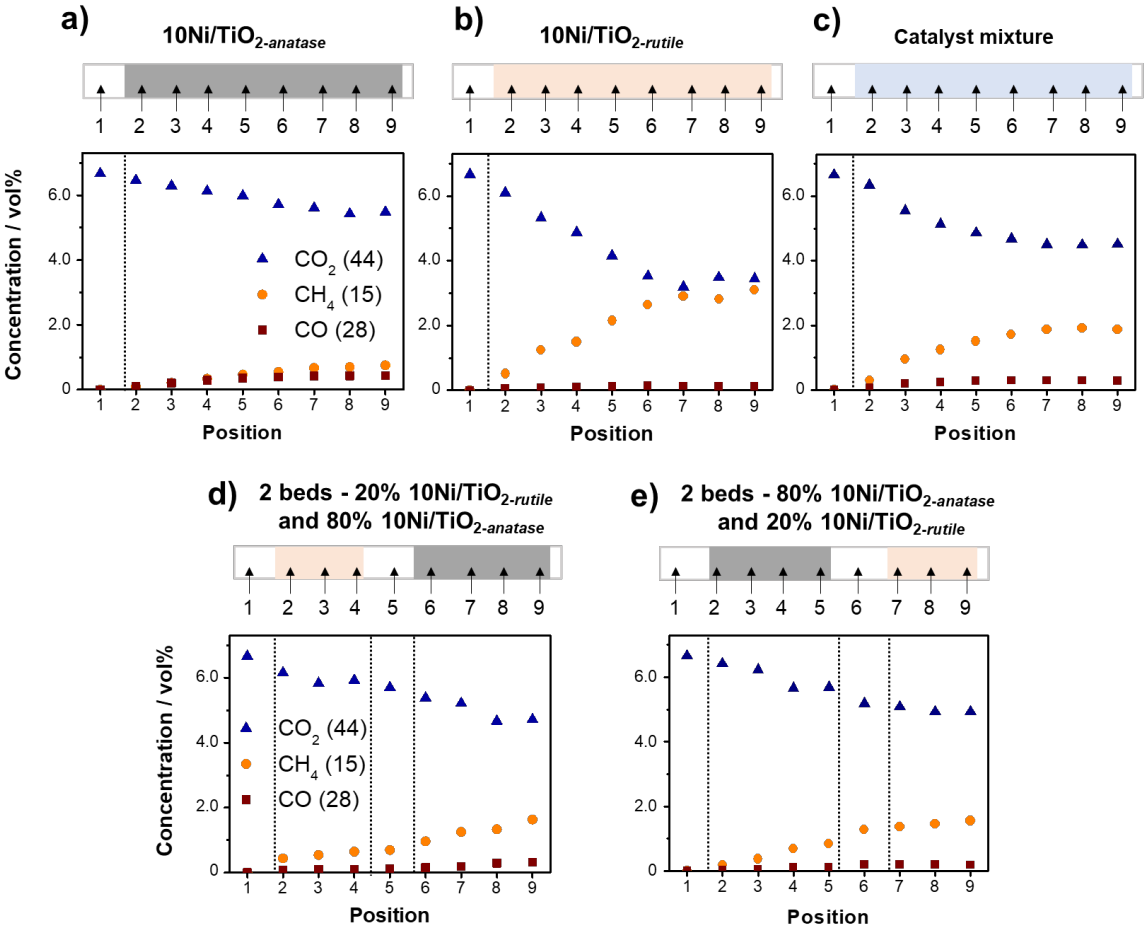

Figure 7. Space-resolved gas sampling for: a) 10Ni/$TiO_{2\text{-}anatase}$; b) 10Ni/$TiO_{2\text{-}rutile}$; c) catalyst mixture 10Ni/$TiO_{2\text{-}anatase}$ (80%) +10Ni/$TiO_{2\text{-}rutile}$ (20 %); d) 2 beds – 20% 10Ni/$TiO_{2\text{-}rutile}$ and 80% 10Ni/$TiO_{2\text{-}anatase}$; and e) 2 beds – 80% 10Ni/$TiO_{2\text{-}anatase}$ and 20% 10Ni/$TiO_{2\text{-}rutile}$. (blue: CO_2; orange: CH_4; and brown: CO (the contribution from CO_2 has been subtracted)). MS profiles (a.u.) along the catalyst bed were converted into concentration profiles (in vol. %) by using the inlet and outlet gas concentrations measured by FTIR.

3.4 Surface species analysis by DRIFTS operando

For surface species analysis by DRIFTS *operando* during CO_2 methanation, the following conditions were used: P_{total} = 1 bar, T = 280-340 °C; CO_2/H_2 = 1/4; WHSV = 336 NmL_{CO2} h^{-1} g^{-1}. These experiments were performed after reducing the catalyst under H_2 at 400 °C for 1 h. Under these conditions, 10Ni/$TiO_{2\text{-}anatase}$, 10Ni/$TiO_{2\text{-}rutile}$ and the catalyst mixture 80% 10Ni/$TiO_{2\text{-}anatase}$ + 20% 10Ni/$TiO_{2\text{-}rutile}$ were studied. First, the relative rates were measured at 280 °C, and under these conditions, a synergistic effect was also observed, as compared to weighted activities (Figure S10). A series of experiments was also performed at different temperatures to calculate the apparent activation energy (SI.2, Table S7). The calculated activation energies were 80 (10Ni/$TiO_{2\text{-}anatase}$), 105 (10Ni/$TiO_{2\text{-}rutile}$), 133 (10Ni/$TiO_{2\text{-}P25}$) and 85.5 kJ.mol^{-1} (catalyst mixture). Figure 8a shows the spectra for the 10Ni/$TiO_{2\text{-}rutile}$ catalyst at various temperatures between 50 and 280 °C taken in the DRIFTS cell under a CO_2+H_2 feed. Only the large band of CO_2(g) at 2360 cm^{-1} is visible for all the temperatures, whereas the CH_4(g) band at 3050 cm^{-1} starts to appear at 260 °C. There are no visible surface species on 10Ni/$TiO_{2\text{-}rutile}$. If, at 280 °C, H_2 is removed from the gas mixture, two large bands at 1875 and 2024 cm^{-1} appear, characteristic of multi-bonded and linear CO on Ni, respectively. These bands disappeared when H_2 was added again to the gas mixture, meaning that nickel carbonyl species are reversibly formed when H_2 is removed (Figure S11). DRIFTS spectra were also recorded at various temperatures with 10Ni/$TiO_{2\text{-}anatase}$ (Figure 8b). In that case, carbonyls adsorbed on Ni are visible under a CO_2+H_2 feed, exhibiting two characteristic bands at 1842 cm^{-1} for multi-bonded nickel carbonyl and 2070 cm^{-1} for linear nickel carbonyl species. Surprisingly, the CO adsorbed on Ni with the mixture of H_2/CO_2 is slowly removed when H_2 is not present in the gas mixture (Figure S12). Ni-CO species are still present 5 min after removing H_2, and they only disappear after 4 h.

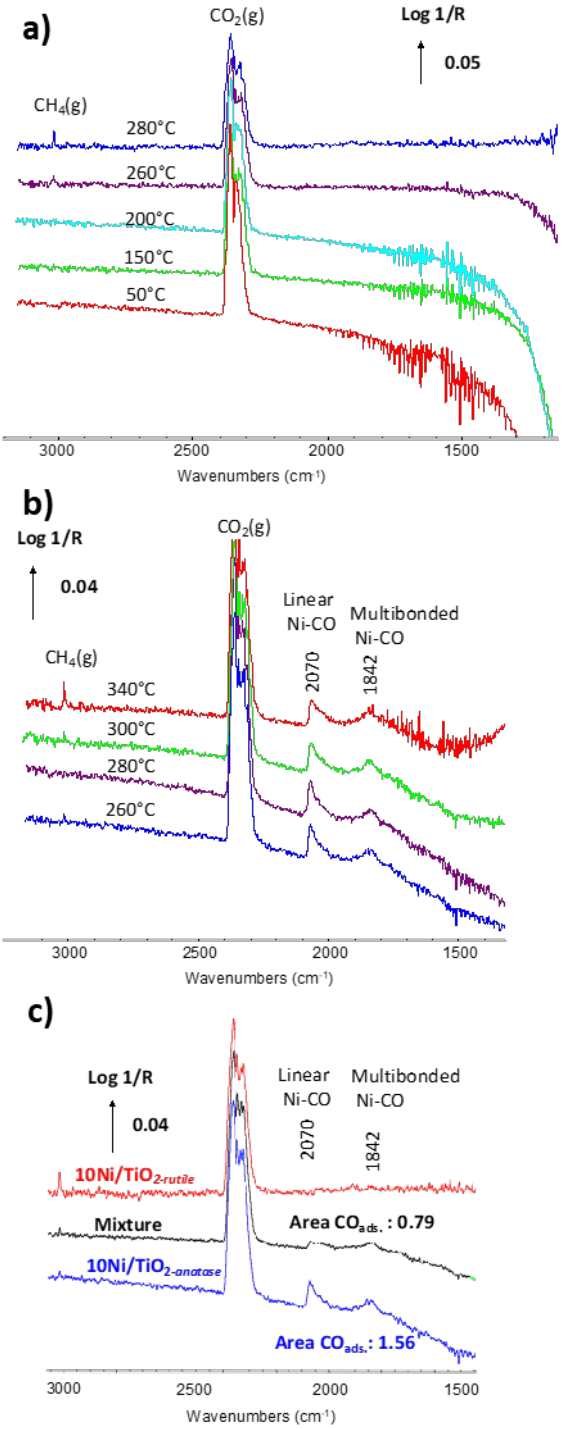

Figure 8 DRIFTS spectra recorded under 2% CO_2 + 8% H_2 (1 bar) for: a) 10Ni/$TiO_{2\text{-}rutile}$ at various temperatures; b) 10Ni/$TiO_{2\text{-}anatase}$ at various temperatures; and c) 10Ni/$TiO_{2\text{-}rutile}$, 10Ni/$TiO_{2\text{-}anatase}$ and the catalyst mixture 80% 10Ni/$TiO_{2\text{-}anatase}$ + 20% 10Ni/$TiO_{2\text{-}rutile}$ at 280°C. (WHSV = 336 NmL_{CO2} h^{-1} g^{-1}).

This contrasts with the data collected over the 10Ni/$TiO_{2\text{-}rutile}$ catalyst, possibly due to differences in CO_2 adsorption or dissociation rates or CO desorption rate (and the gradual oxidation of Ni particles by CO_2 in the absence of H_2). There is no visible formation of formate or carbonate species on nickel. These results contrast with those obtained by Bao *et al*. at much lower temperature (*i.e*. 75 °C) [33], who observed the formation of hydrogenocarbonate species on both Ni/$TiO_{2\text{-}rutile}$ and Ni/$TiO_{2\text{-}anatase}$ catalysts. The higher temperatures used here likely led to lower surface coverage of these weakly bound species. The study by Bao *et al*. was also conducted at atmospheric pressure, but using a catalyst reduced 4 h at 500°C and at a higher WHSV (2400 NmL_{CO2} g^{-1} h^{-1}). The fact that such adsorbed species were not observed in this study could thus be related to: i) a low surface coverage; or ii) the reduction conditions. For this latter possibility, Panagiotopoulou *et al*. have recently shown that during CO_2 methanation formate species appeared after prolonged catalyst reduction [62]. The same operando DRIFTS experiments were performed with the mixture of catalysts. Figure 8c shows a comparison of the three catalysts. A quantitative analysis of the sample spectra at 280 °C (Figure 8.c) is only valid if the materials exhibit similar scattering and absorption coefficient, leading to similar optical pathlengths. This can be assumed to be true in the present case, since a mixture of the same loading of Ni supported on two titania polymorphs are considered. For the catalyst mixture 80% 10Ni/$TiO_{2\text{-}anatase}$ + 20% 10Ni/$TiO_{2\text{-}rutile}$, CO adsorbed on metallic Ni is still visible, but the band area of adsorbed CO has a calculated value of 0.79 for the mixture, when a value of 1.25 (= 0.8 * 1.56) would be expected for an 80% dilution of the signal obtained on the pure 10Ni/$TiO_{2\text{-}anatase}$. This important observation corroborates the fact that the 10Ni/$TiO_{2\text{-}rutile}$ assisted the hydrogenation of the CO(ads) on the 10Ni/$TiO_{2\text{-}anatase}$. This result enables to unravel the origin of one of the synergetic effects between 10Ni/$TiO_{2\text{-}rutile}$ and 10Ni/$TiO_{2\text{-}anatase}$.

3.5 H_2-TPD experiments and catalytic tests to assess hydrogen spillover

The results from catalyst characterization, catalytic study, operando DRIFTS and MS study can be summarized as follows:

- 10Ni/$TiO_{2\text{-}anatase}$ and 10Ni/$TiO_{2\text{-}rutile}$ present similar Ni particle size before and after catalysis, and from XPS analyses, similar metal support interactions (except maybe at the interface where should be located the active sites);
- for pure catalysts, the activity, selectivity and stability for CO_2 methanation are higher on Ni/$TiO_{2\text{-}rutile}$ than those on 10Ni/$TiO_{2\text{-}anatase}$;
- when a mixture of these two catalysts is used, a synergistic effect is observed, since the measured rate of the mixture is higher than the corresponding calculated weighted rate;
- the two catalysts do not need to be in physical contact for the synergistic effect to occur (configuration **C1**);
- during the methanation reaction, adsorbed CO is accumulating on Ni/$TiO_{2\text{-}anatase}$, and one role of the Ni/$TiO_{2\text{-}rutile}$ could be to assist the hydrogenation of this adsorbed CO.

Taken together, these results suggest that: i) these catalysts could contain mainly interfacial actives sites; ii) Ni/$TiO_{2\text{-}anatase}$ is a more selective but less active RWGS reaction catalyst compared to Ni/$TiO_{2\text{-}rutile}$ (hypothesis independently checked, see Figure S12), which is a necessary step for methanation; iii) methanation of CO, generally recognized as the rate-determining step of the reaction [30, 63-66], should be faster on Ni/$TiO_{2\text{-}rutile}$ [33], iv) hydrogen spillover, which occurs fast and at relatively large distances on reducible supports, by surface species but also by gas-phase radicals [67-69], could be involved in the process, by assisting the CO_2 hydrogenation steps on Ni/$TiO_{2\text{-}anatase}$; and v) the optimal anatase/rutile ratio can arise from the balance of the reaction rates for the H-spillover and CO_2 methanation.

Concerning hydrogen spillover, it is worth mentioning that it has already been proposed as the explanation of the synergy between Pd/γ-Al_2O_3 and Rh/γ-Al_2O_3 catalysts in CO_2 methanation [70]. In that study, the authors have shown that although Pd/γ-Al_2O_3 is inactive at 200 °C, the activity of mechanical mixtures of the two catalysts was up to 50 % higher than that of the pure Rh/γ-Al_2O_3 catalyst. While Pd/γ-Al_2O_3 alone could not hydrogenate the Pd-CO adsorbed species, the presence of Rh/γ-Al_2O_3 significantly increased the reactivity of Pd-CO species, which was proposed to account for the observed synergistic effect, *via* hydrogen spillover. Synergies associated to H-spillover were also reported for mechanical mixtures of Rh/γ-Al_2O_3 (methanation catalyst) and Ni/C (spillover catalyst) [71], for Ni-Ru/SiO_2-La_2O_3 catalysts (Ni: methanation catalyst, and Ru: spillover catalyst) [72], or for Co-Pt/SiO_2 catalysts [73, 74]. In this latter case, it was shown that the H-spillover (from Pt to Co) significantly enhance the reduction of Co. This effect could be also important in our case since: i) it is known that Ni deactivation can occur due to coke formation [75] or formation of Ni-hydroxide by reaction with water [63], and ii) the deactivation observed for pure Ni/$TiO_{2\text{-}anatase}$ is suppressed when using the catalyst mixture (see Figure S7). Another implication of H-spillover in CO_2 methanation on Ru/CeO_2 [76] and Ni/MgO [77] catalysts is related to H-assisted H_2O removal.

H_2-TPD of the three catalysts, 10Ni/$TiO_{2\text{-}anatase}$, 10Ni/$TiO_{2\text{-}rutile}$ and the physical mixture, were performed after hydrogen reduction at 400 °C in order to quantify the spillover of hydrogen. The total amounts of H_2 adsorbed on these three catalysts were 29.6, 50.3 and 32.9 $\mu mol.g^{-1}$ for 10Ni/$TiO_{2\text{-}anatase}$, 10Ni/$TiO_{2\text{-}rutile}$ and the mixture, respectively. Concerning the supports (Figure 9), higher amounts of H_2 were observed for the $TiO_{2\text{-}rutile}$ (4 $m^2\ g^{-1}$) than for $TiO_{2\text{-}anatase}$ (10 $m^2\ g^{-1}$). The heterolytic H_2 dissociation (leading to a hydride and a hydroxyl) on $TiO_{2\text{-}rutile}$ has been reported to proceed much more easily (E_a = 8.5 kcal mol^{-1}) than on $TiO_{2\text{-}anatase}$ (E_a = 24 kcal mol^{-1}) [78]. For $TiO_{2\text{-}rutile}$, the hydride produced by the H_2 heterolytic activation can transfer from Ti to O with activation energy of 22.8 kcal mol^{-1}, yielding the homolytic products. For the

catalysts, higher amounts of H_2 were observed for the 10Ni/$TiO_{2\text{-}rutile}$ compared to 10Ni/$TiO_{2\text{-}anatase}$. Theoretical calculations have shown that although H_2 desorption is difficult on a stoichiometric TiO_2 surface, it becomes easier (and favored upon H_2O desorption) with an increase in O_v, which are generated by H_2O desorption [79]. Two main desorption peaks are observed at ~190 and ~300 °C. The presence of these two peaks in Ni/TiO_2 catalysts has already been reported [80]. The peak at lower temperature (190 °C) can be attributed to hydrogen chemisorbed at the surface of the Ni particles [20], and to reverse hydrogen spillover. The presence of a peak at higher temperatures has been discussed in several studies dealing with hydrogen spillover on TiO_2 supports, it is ascribed to H-spillover associated with the support [81, 82]. The desorption of hydrogen adsorbed at interfacial sites located at the metal-support interface has also be invoked [83]. These analyses point to a higher H-spillover on 10Ni/$TiO_{2\text{-}rutile}$ than on 10Ni/$TiO_{2\text{-}anatase}$. On Ru/TiO_2 catalysts, the opposite situation was observed [53], which highlights the importance of the intimate interaction between the metal and the support on the jump of the hydride from the metal to the support.

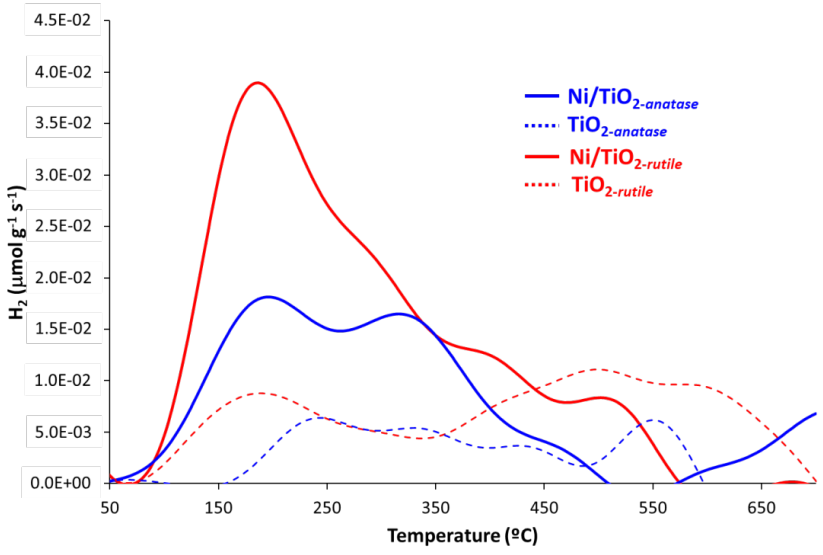

Figure 9. H_2-TPD profiles over $TiO_{2\text{-}anatase}$, 10Ni/$TiO_{2\text{-}anatase}$, $TiO_{2\text{-}rutile}$ and 10Ni/$TiO_{2\text{-}rutile}$.

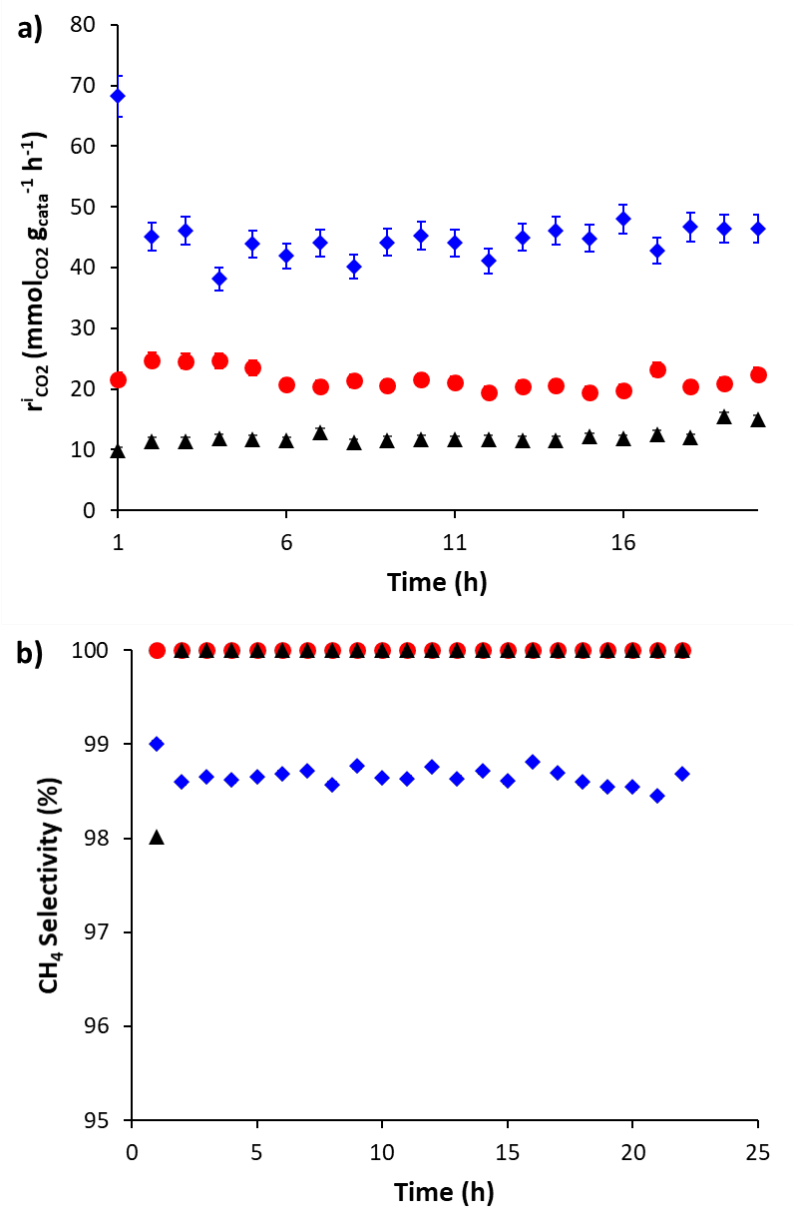

Figure 10. Comparison of: a) CO_2 consumption rates at the inlet of the reactor; and b) CH_4 selectivity at 260 °C of 10Ni/$TiO_{2\text{-}P25}$ diluted with 1.8 g of SiC (black triangles), diluted in $TiO_{2\text{-}rutile}$ (red circles) - 0.2g 10Ni/$TiO_{2\text{-}P25}$ + 1g $TiO_{2\text{-}rutile}$ (+ 0.8 g SiC), and diluted in $TiO_{2\text{-}anatase}$ (blue diamonds) - 0.2g 10Ni/$TiO_{2\text{-}P25}$ + 1g $TiO_{2\text{-}anatase}$ (+ 0.8 g SiC).

Since spillover is often postulated when a dilution of the catalyst leads to an activity increase, we performed two experiments starting from the 10Ni/$TiO_{2\text{-}P25}$ catalyst, measuring the CO_2 consumption rate evolution upon dilution of the catalyst with either $TiO_{2\text{-}rutile}$ or $TiO_{2\text{-}anatase}$ (in addition to SiC). The increase of the rate with higher degrees of dilution can be understood if one admits that the reaction also involves the support (because of spillover hydrogen) in addition to reactivity occurring on the sites of the Ni/TiO_2 particles. The results of these experiments performed at 260 °C in order to better quantify differences are shown on Figure 10 and Table S11.

For both tests performed with diluted catalysts, the rate increases, confirming hydrogen spillover. The rate increase is significantly higher when the dilution is performed with the $TiO_{2\text{-}anatase}$ support, with a calculated TOF = 0.0197 s^{-1}, which is one of the highest reported for Ni-catalyzed CO_2 methanation at this temperature and GHSV (see Table S12 for comparison with reference catalysts). We independently verified that an increase in CO_2 consumption rates was also observed after dilution of the 10Ni/$TiO_{2\text{-}rutile}$ catalyst in pure $TiO_{2\text{-}anatase}$ support (Figure S14 and Table S13). These data suggest that CO_2 is also hydrogenated on the Ni-free $TiO_{2\text{-}anatase}$ and much less on the Ni-free $TiO_{2\text{-}rutile}$. On $TiO_{2\text{-}anatase}$, however, the reaction seems to be slightly less selective (Table S11) since small amounts of CO are produced.

These results can be rationalized by: i) an easier spillover hydrogen species diffusion on $TiO_{2\text{-}anatase}$ than on $TiO_{2\text{-}rutile}$ and/or ii) the higher specific surface area of $TiO_{2\text{-}anatase}$ (10 m^2 g^{-1}) compared to $TiO_{2\text{-}rutile}$ (4 m^2 g^{-1}). To evaluate the impact of the support surface area we also performed a dilution test with the 10Ni/$TiO_{2\text{-}P25}$ catalyst and only 0.4 g of $TiO_{2\text{-}anatase}$ to be at isosurface with 1 g of $TiO_{2\text{-}rutile}$ (Table S11). In that case the CO_2 consumption rate increases compared to pure 10Ni/$TiO_{2\text{-}P25}$ (15.0 $mmol_{CO2}$ g_{cat}^{-1} h^{-1}) is not so high. Indeed, the rate is 25.0 $mmol_{CO2}$ g_{cat}^{-1} h^{-1} (0.4 g of $TiO_{2\text{-}anatase}$) instead of 45.4 $mmol_{CO2}$ g_{cat}^{-1} h^{-1} (1 g of $TiO_{2\text{-}anatase}$), which is still higher than with 1 g of $TiO_{2\text{-}rutile}$ (21.3 $mmol_{CO2}$ g_{cat}^{-1} h^{-1}).

If the bare supports are considered, the mechanism for hydrogen atom diffusion has been investigated by DFT [84-86]. Three competing processes have been taken into account, namely, migration of H on the surface, diffusion of H into the bulk, and hydrogen desorption. On both supports, diffusion of H into the bulk is both kinetically and thermodynamically favorable. Activation barriers for bulk migration of 102 and 67 kJ mol^{-1} have been reported for $TiO_{2\text{-}rutile}$ and $TiO_{2\text{-}anatase}$, respectively. This latter result corroborates our experimental findings. We can thus propose that Ni-initiated hydrogen spillover on Ni/TiO_2 creates active sites on the TiO_2 bare support for CO_2 hydrogenation. The generation thanks to H-spillover of active hydrogenation sites on TiO_2 (O_v created by partial reduction of TiO_2) has already been reported during the Ag/TiO_2 catalyzed hydrodeoxygenation of guaiacol [87] and the Fe/TiO_2 catalyzed ammonia synthesis [88].

It thus appears that the origin of the synergetic effect between TiO_2 crystalline phases in the Ni/TiO_2 catalyzed CO_2 methanation reaction comes from hydrogen activation. The $Ni/TiO_{2\text{-}rutile}$ catalyst is much more active for CO_2 reduction to methane than $Ni/TiO_{2\text{-}anatase}$ for a CO_2/H_2 ratio of 1/4 and 1/1. On the other hand, $Ni/TiO_{2\text{-}anatase}$ is more selective for the RWGS reaction catalyst, and the diffusion of H-species is easier on the $TiO_{2\text{-}anatase}$ support than on $TiO_{2\text{-}rutile}$. Thus, in a catalyst mixture, the H-species resulting from the spillover on the $Ni/TiO_{2\text{-}rutile}$ catalyst should have the tendency to accumulate on the $TiO_{2\text{-}anatase}$ support (Scheme 1).

The contact between the two supports is actually not necessary since gas phase hydrogen spillover can occur [66-68, 89-91]. Even if thermodynamically the gas phase H spillover concentration should be very low [92], it should permit a fast formation of H species adsorbed on the support. Additionally, the water present in the gas phase could be involved in the transport process maybe *via* the reactor walls or the quartz wool used to separate the catalyst beds [93].

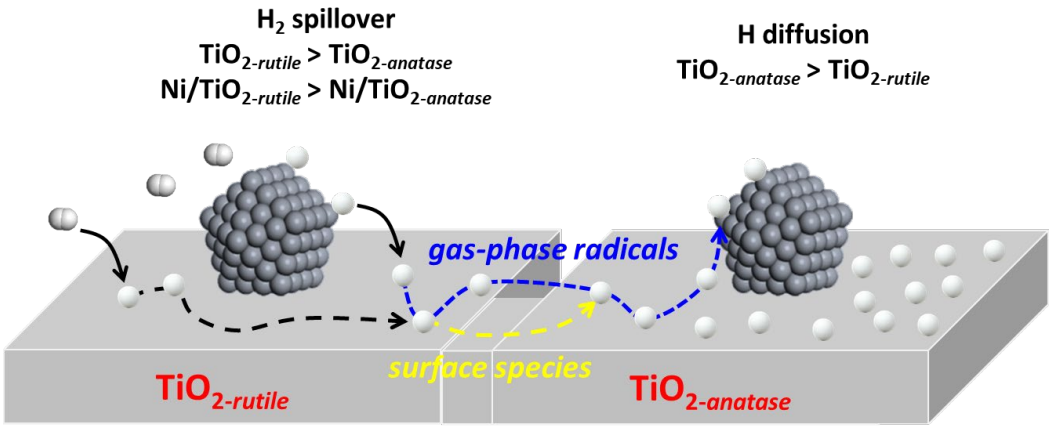

Scheme 1. Hydrogen spillover and H diffusion in a Ni/$TiO_{2\text{-}rutile}$ - Ni/$TiO_{2\text{-}anatase}$ catalyst mixture.

When these H species have reached the $TiO_{2\text{-}anatase}$ support, the CO_2 hydrogenation is greatly improved on the Ni/$TiO_{2\text{-}anatase}$ catalyst, the methane being formed even from the support alone, and catalyst deactivation is reduced. The part of CH_4 formed directly on the TiO_2 support is however relatively low. Thus, we compare the CO_2 conversion at 260 °C for the 10Ni/$TiO_{2\text{-}rutile}$ catalyst (200 mg), the 10Ni/$TiO_{2\text{-}rutile}$ catalyst (60 mg, corresponding to 30% in weight) mixed with 140 mg of $TiO_{2\text{-}anatase}$ (corresponding to 70% in weight), and the Ni/$TiO_{2\text{-}rutile}$ catalyst (60 mg, corresponding to 30% in weight) mixed with 140 mg of Ni/$TiO_{2\text{-}anatase}$ (corresponding to 70% in weight). The results, presented on Table S13, clearly show that the conversion improvement linked to the Ni on Ni/$TiO_{2\text{-}anatase}$ is much higher than the one linked to the $TiO_{2\text{-}anatase}$ support itself. The precise role of the H species is still unclear, but it is worth mentioning that TiO_2 reduction by hydrogen spillover has been reported [94-96]. Additionally, it was reported that on Rh catalyst supported on CeO_2 (another reducible support), the fraction of CO that undergoes dissociation increases significantly as the CeO_2 surface is reduced [97]. The fact that the TOF of the catalyst mixture is significantly higher than that of the Ni/$TiO_{2\text{-}P25}$ catalyst could be related to the lower specific surface area of the supports used in the mixture compared

to $TiO_{2\text{-}P25}$, and to Ni particle proximity, which should be higher for the mixture of catalysts. These two characteristics should favor the hydrogen spillover. Finally, considering the fact that Ni particles in $Ni/TiO_{2\text{-}anatase}$ and $Ni/TiO_{2\text{-}rutile}$ catalysts present similar sizes without TiO_x overlayers, and similar electronic interaction with the supports, we can propose that these catalysts should contain mainly interfacial actives sites [98]. The importance of the metal-support interface in Ni-catalyzed CO_2 hydrogenation has been discussed [57,77,99,100]. For CO_2 methanation, the role of the active sites located at the Ni-support interface has been studied by DFT and *operando* DRIFT analyses, and different implications related to the reaction mechanism have been proposed.

On Ni/ZrO_2 catalysts, hydrogen species generated by hydrogen spillover could contribute to the formation of O_v on the ZrO_2 surface, which enhance CO_2 adsorption and activation [99]. It was also proposed that the interaction of the Ni-ZrO_2 interface with adsorbed CO was strong enough to facilitate its further hydrogenation to CH_4 [57]. For the Sabatier reaction on Ni/MgO catalysts, it was shown by DFT that the presence of the MgO support is beneficial for the OH removal from intermediate species, and consequently for H_2O formation during CO_2 methanation, due to hydrogen-spillover and the strong OH adsorption on the MgO support [77]. On Ni/CeO_2 catalysts [101], it was recently proposed that, as in the case of Ni/ZrO_2 catalysts [99], H-spillover from Ni to CeO_2 can lead to a partial reduction of CeO_2 and generation of O_v at the metal-support interface region. A linear correlation between the CO_2 methanation reaction rate and the number of O_v was reported. This suggests the involvement of surface O_v in CO_2 adsorption and activation [102]. A similar phenomenon could occur on TiO_2, another reducible oxide. Such a phenomenon could be at the origin of the difference of reactivity between $10Ni/TiO_{2\text{-}anatase}$ and $10Ni/TiO_{2\text{-}rutile}$ catalysts. Indeed, it was shown by DFT that the O_v formation energy is much lower on $TiO_{2\text{-}rutile}$ rutile than on $TiO_{2\text{-}anatase}$ [103]. Thus, the

higher H-spillover on 10Ni/$TiO_{2\text{-}rutile}$ than on 10Ni/$TiO_{2\text{-}anatase}$ could result in a higher concentration of O_v on the 10Ni/$TiO_{2\text{-}rutile}$ catalyst, and consequently a higher activity.

Finally, as far as Ni/TiO_2 catalyst stability is concerned, it is worth mentioning that it has been reported that highly active hydrogen species resulting from spillover that diffuse on Ni catalyst surface lead to the hydrogenation of the coke precursor species adsorbed on the catalyst [104,105], and to the reduction of nickel oxide [106]. Such phenomena could explain why the use of mixture of TiO_2 phases allows limiting catalyst deactivation (Fig. S6b for 10Ni/$TiO_{2\text{-}P25}$).

4. Conclusion

Nickel catalysts (10% w/w) were prepared on $TiO_{2\text{-}rutile}$, $TiO_{2\text{-}anatase}$ and $TiO_{2\text{-}P25}$. The catalysts prepared on $TiO_{2\text{-}rutile}$ and $TiO_{2\text{-}anatase}$ present a similar Ni particle size (~ 30 nm) before and after CO_2 methanation, as well as similar metal-support interactions. The 10Ni/$TiO_{2\text{-}P25}$ presents smaller particle size (~ 20 nm). The CO_2 consumption rate measured at the inlet of the reactor of 10Ni/$TiO_{2\text{-}anatase}$, 10Ni/$TiO_{2\text{-}rutile}$, 10Ni/$TiO_{2\text{-}P25}$ and a physical mixture of 30% 10Ni/$TiO_{2\text{-}rutile}$ + 70% 10Ni/$TiO_{2\text{-}anatase}$ show that a synergistic effect operates when a mixture of the crystal phases of TiO_2 is used as a support in the Ni/TiO_2-catalyzed methanation reaction. The synergy observed using a mixture of catalysts could also occur *even if the two catalysts are not in physical contact*. H_2-TPD analyses and methanation tests performed with diluted catalysts have shown that hydrogen spillover is more pronounced on the Ni/$TiO_{2\text{-}rutile}$ catalyst. DRIFTS operando analyses have shown that adsorbed CO is accumulating on Ni/$TiO_{2\text{-}anatase}$ but not on Ni/$TiO_{2\text{-}rutile}$. The synergy between the two catalysts can be rationalized as follows: i) the Ni/$TiO_{2\text{-}rutile}$ catalyst is active and selective for CO_2 methanation and also for hydrogen activation; ii) the Ni/$TiO_{2\text{-}anatase}$ is poorly active for the CO_2 methanation and RWGS, and the

$TiO_{2\text{-}anatase}$ support is more efficient than $TiO_{2\text{-}rutile}$ for diffusion of H species; iii) when the two catalysts are used together, the H species diffuse from $Ni/TiO_{2\text{-}rutile}$ to $Ni/TiO_{2\text{-}anatase}$; iv) the H-enriched $Ni/TiO_{2\text{-}anatase}$ catalyst becomes very active for CO_2 methanation. The optimal $TiO_{2\text{-}anatase}/TiO_{2\text{-}rutile}$ ratio (between 0.4 and 0.8) is achieved through a control of the balance of the spillover, CO_2 methanation and deactivation rates. Finally, the higher TOF obtained with catalyst mixtures compared to $Ni/TiO_{2\text{-}P25}$ suggests that interfacial sites, presumably involving O_v, should be involved in this reaction. Our results that confirm the essential role of the support for Ni-based CO_2 methanation catalysts [107], can also be put into perspective to propose an explanation of the support effect (rutile *vs* anatase) observed on Co/TiO_2 catalysts for Fischer-Tropsch synthesis, for which a similar synergistic effect has been observed without being clearly explained [108, 109]. DFT calculations are in course to reveal the mechanism of the hydrogenation at the interfacial active sites and on the bare $TiO_{2\text{-}anatase}$ support, and to clarify the possible role(s) of the H species resulting from spillover (H-assisted hydrogenation steps, H-assisted water desorption or H-assisted Ni reduction).

Notes

The authors declare no competing financial interest.

Acknowledgements.

This work was financially supported by "Région Occitanie" through a laboratory and company contract "HYDROMET: Renewable CO_2 hydrogenation for methane production" (N°15065590). B.F.M. acknowledges the exploratory project under the Fundação para a Ciência e a Tecnologia (FCT, Portugal) Investigator Programme (ref. IF/00301/2015) with financial support from FCT/MCTES, through national funds (PIDDAC).

References:

[1] D. Y. C. Leung, G. Caramanna, M. M. Maroto-Valer, An overview of current status of carbon dioxide capture and storage technologies, Renew. Sus. Energ. Rev., 39 (2014) 426-443.

[2] M. Bui, C. S. Adjiman, A. Bardow, E. J. Anthony, A. Boston, S. Brown, P. S. Fennell, S. Fuss, A. Galindo, L. A. Hackett, et al. Carbon capture and storage (CCS): the way forward, Energy Environ. Sci., 11 (2018) 1062-1176.

[3] J. G. Vitillo, B. Smit, L. Gagliardi, Introduction: Carbon Capture and Separation, Chem. Rev., 117 (2017) 9521-9523.

[4] M. Mikkelsen, M. Jørgensen, F. C. Krebs, The teraton challenge. A review of fixation and transformation of carbon dioxide, Energy Environ. Sci., 3 (2010) 43-81.

[5] T. Sakakura, J.-C. Choi, H. Yasuda, Transformation of Carbon Dioxide, Chem. Rev., 107 (2007) 2365-2387.

[6] J. Artz, T. E. Müller, K. Thenert, J. Kleinekorte, R. Meys, A. Sternberg, A. Bardow, W. Leitner, Sustainable Conversion of Carbon Dioxide: An Integrated Review of Catalysis and Life Cycle Assessment, Chem. Rev., 118 (2018) 434-504.

[7] G. Centi, S. Perathoner, Opportunities and prospects in the chemical recycling of carbon dioxide to fuels, Catal. Today, 148 (2009) 191-205.

[8] K. Ghaib, K. Nitz, F.-Z. Ben-Fares, Chemical Methanation of CO_2: A Review, ChemBioEng Rev., 3 (2016) 266-275.

[9] P. Frontera, A. Macario, M. Ferraro, P. Antonucci, Supported Catalysts for CO_2 Methanation: A Review, Catalysts, 7 (2017) 59.

[10] W. Wei, G. Jinlong, Methanation of carbon dioxide: an overview, Front. Chem. Sci. Eng., 5 (2011) 2-10.

[11] A. Solis-Garcia, J. C. Fierro-Gonzalez, Mechanistic Insights into the CO_2 Methanation Catalyzed by Supported Metals: A Review, J. Nanosci. .Nanotechnol., 19 (2019) 3110-3123.

[12] M. Bailera, P. Lisbona, L. M. Romeo, S. Espatolero, Power to Gas projects review: Lab, pilot and demo plants for storing renewable energy and CO_2, Renew. Sus. Energ. Rev., 69 (2017) 292-312.

[13] K. Ghaib, F.-Z. Ben-Fares, Power-to-Methane: A state-of-the-art review, Renew. Sus. Energ. Rev., 81 (2018) 433-446.

[14] M. Thema, F. Bauer, M. Sterner, Power-to-Gas: Electrolysis and methanation status review, Renew. Sus. Energ. Rev., 112 (2019) 775-787.

[15] X. Guo, A. Traitangwong, M. Hu, C. Zuo, V. Meeyoo, Z. Peng, C. Li, Carbon Dioxide Methanation over Nickel-Based Catalysts Supported on Various Mesoporous Material, Energ. Fuels, 32 (2018) 3681-3689.

[16] J. Martínez, E. Hernández, S. Alfaro, R. López Medina, G. Valverde Aguilar, E. Albiter, M. A. Valenzuela, High Selectivity and Stability of Nickel Catalysts for CO_2 Methanation: Support Effects, Catalysts, 9 (2018) 24.

[17] K. Stangeland, D. Kalai, H. Li, Z. Yu, CO_2 Methanation: The Effect of Catalysts and Reaction Conditions, Energy Procedia, 105 (2017) 2022-2027.

[18] I. Sreedhar, Y. Varun, S. A. Singh, A. Venugopal, B. M. Reddy, Developmental trends in CO_2 methanation using various catalysts, Catal. Sci. Technol., 9 (2019) 4478-4504.

[19] J. H. Jensen, J. M. Poulsen, N. U. Andersen, From coal to clean energy, Nitrogen+Syngas, (2011) 310.

[20] J. Liu, C. Li, F. Wang, S. He, H. Chen, Y. Zhao, M. Wei, D. G. Evans, X. Duan, Enhanced low-temperature activity of CO_2 methanation over highly-dispersed Ni/TiO_2 catalyst, Catal. Sci. Technol., 3 (2013) 2627-2633.

[21] Y. Wang, Y. Xu, Q. Liu, J. Sun, S. Ji, Z.-j. Wang, Enhanced low-temperature activity for CO_2 methanation over NiMgAl/SiC composite catalysts, J. Chem. Technol. Biotechnol., 94 (2019) 3780-3786.

[22] S. Tada, T. Shimizu, H. Kameyama, T. Haneda, R. Kikuchi, Ni/CeO_2 catalysts with high CO_2 methanation activity and high CH_4 selectivity at low temperatures, Int. J. Hydrogen Energ., 37 (2012) 5527-5531.

[23] L. Bian, L. Zhang, R. Xia, Z. Li, Enhanced low-temperature CO_2 methanation activity on plasma-prepared Ni-based catalyst, J. Nat. Gas Sci. Eng., 27 (2015) 1189-1194.

[24] W. L. Vrijburg, E. Moioli, W. Chen, M. Zhang, B. J. P. Terlingen, B. Zijlstra, I. A. W. Filot, A. Züttel, E. A. Pidko, E. J. M. Hensen, Efficient Base-Metal NiMn/TiO_2 Catalyst for CO_2 Methanation, ACS Catal., 9 (2019) 7823-7839.

[25] X. Guo, H. He, A. Traitangwong, M. Gong, V. Meeyoo, P. Li, C. Li, Z. Peng, S. Zhang, Ceria Imparts Superior Low Temperature Activity to Nickel Catalysts for CO_2 Methanation, Catal. Sci. Technol., 9 (2019) 5636-5650.

[26] S. Bagheri, N. Muhd Julkapli, S. Bee Abd Hamid, Titanium Dioxide as a Catalyst Support in Heterogeneous Catalysis, Sci. World J., (2014) 727496.

[27] K. Bourikas, C. Kordulis, A. Lycourghiotis, Titanium Dioxide (Anatase and Rutile): Surface Chemistry, Liquid–Solid Interface Chemistry, and Scientific Synthesis of Supported Catalysts, Chem. Rev., 114 (2014) 9754-9823.

[28] U. Diebold, The Surface Science of Titanium Dioxide, Surf. Sci. Rep., 48 (2003) 53-229.

[29] W. Li, G. Zhang, X. Jiang, Y. Liu, J. Zhu, F. Ding, Z. Liu, X. Guo, C. Song, CO_2 Hydrogenation on Unpromoted and M-Promoted Co/TiO_2 Catalysts (M = Zr, K, Cs): Effects of Crystal Phase of Supports and Metal − Support Interaction on Tuning Product Distribution, ACS Catal., 9 (2019) 2739-2751.

[30] M. R. Prairie, A. Renken, J. G. Highfield, K. Ravindranathan Thampi, M. Grätzel, A fourier transform infrared spectroscopic study of CO_2 methanation on supported ruthenium, J. Catal., 129 (1991) 130-144.

[31] A. Kim, C. Sanchez, G. Patriarche, O. Ersen, S. Moldovan, A. Wisnet, C. Sassoye, D. P. Debecker, Selective CO_2 methanation on Ru/TiO_2 catalysts: unravelling the decisive role of the TiO_2 support crystal structure, Catal. Sci. Technol., 6 (2016) 8117-8128.

[32] A. Kim, D. P. Debecker, F. Devred, V. Dubois, C. Sanchez, C. Sassoye, CO_2 methanation on Ru/TiO_2 catalysts: On the effect of mixing anatase and rutile TiO_2 supports, Appl. Catal. B., 220 (2018) 615-625.

[33] Y. Lin, Y. Zhu, X. Pan, X. Bao, Modulating the methanation activity of Ni by the crystal phase of TiO_2, Catal. Sci. Technol., 7 (2017) 2813-2818.

[34] S. Chai, Y. Men, J. Wang, S. Liu, Q. Song, W. An, G. Kolb, Boosting CO_2 Methanation Activity on Ru/TiO_2 Catalysts by Exposing (001) Facets of Anatase TiO_2, J. CO_2 Util., 33 (2019) 242-252.

[35] A. Borodzinski, M. Bonarowska, Relation between Crystallite Size and Dispersion on Supported Metal Catalysts, Langmuir, 13 (1997) 5613-5620.

[36] A. Champon, A. Bengaouer, S. Chaise, S. Thomas, A.-C. Roger, Carbon dioxide methanation kinetic model on a commercial Ni/Al2O3 catalyst, J. CO_2 Util., 34 (2019) 256-265.

[37] K. J. A. Raj, M. G. Prakash, R. Mahalakshmy, T. Elangovan, B. Viswanathan, Liquid Phase Hydrogenation of Nitrobenzene over Nickel Supported on Titania, Chin. J. Catal., 33 (2012) 1299–1305.

[38] M. Xu, S. He, H. Chen, G. Cui, L. Zheng, B. Wang, M. Wei, TiO_{2-x}-modified Ni nanocatalyst with tunable metal-support interaction for water-gas shift reaction, ACS Catal., 7 (2017) 7600-7609.

[39] A. Shukla, R. Kumar Singha, T. Sasaki, S. Adak, S. Bhandari, V. V. D. N. Prasad, A. Bordoloi, R. Bal, Room temperature selective reduction of nitroarenes to azoxy compounds over Ni-TiO_2 catalyst, Mol. Catal. 490 (2020) 110943.

[40] G. Sankar, K. R. Kannan, C. N. R. Rao, Anatase-Rutile Transformation in Fe/TiO_2, Th/TiO_2 and Cu/TiO_2 Catalysts and its Possible Role in Metal-Support Interaction, Catal. Lett., 8 (1991) 27-36.

[41] R. A. Spurr, H. Myers, Quantitative Analysis of Anatase-Rutile Mixtures with an X-Ray Diffractometer, Anal. Chem., 29 (1957) 760-762.

[42] P. Li, J. Liu, N. Nag, P. A. Crozier, Dynamic Nucleation and Growth of Ni Nanoparticles on High-Surface Area Titania, Surf. Sci., 600 (2006) 693-702.

[43] S.-W. Ho, C.-Y. Chu, S.-G. Chen, Effect of Thermal Treatment on the Nickel State and CO Hydrogenation Activity of Titania-Supported Nickel Catalysts, J. Catal., 178 (1998) 34-48.

[44] F.C. Meunier, On the contamination with nickel and nickel tetracarbonyl during FT-IR investigation of catalysts under CO-containing gases, J. Catal., 372 (2019) 388-388.

[45] M. C. Biesinger, B. P. Payne, L. W. M. Lau, A. Gerson, R. S. C. Smart, X-ray Photoelectron Spectroscopic Chemical State Quantification of Mixed Nickel Metal, Oxide and Hydroxide Systems, Surf. Interface Anal., 41 (2009) 324-332.

[46] M. C. Biesinger, B. P. Payne, A. P. Grosvenor, L. W. M. Lau, A. R. Gerson, R. S. C. Smart, Resolving Surface Chemical States in XPS Analysis of First Row Transition Metals, Oxides and Hydroxides: Cr, Mn, Fe, Co and Ni, Appl. Surf. Sci., 257 (2011) 2717-2730.

[47] L. Soriano, I. Preda, A. Gutiérrez, S. Palacín, M. Abbate, A. Vollmer, Surface Effects in the Ni 2p X-Ray Photoemission Spectra of NiO, Phys. Rev. B, 75 (2007) 233417.

[48] B. Zhao, X.-K. Ke, J.-H. Bao, C.-L. Wang, L. Dong, Y.-W. Chen, H.-L. Chen, Synthesis of Flower-Like NiO and Effects of Morphology on Its Catalytic Properties, J. Phys. Chem. C, 113, (2009) 14440-14447.

[49] V. Vonk, N. Khorshidi, A. Stierle, Structure and Oxidation Behavior of Nickel Nanoparticles Supported by YSZ(111), J. Phys. Chem. C, 121 (2017) 2798-2806.

[50] J. Li, Y. Lin, X. Pan, D. Miao, D. Ding, Y. Cui, J. Dong, X. Bao, Enhanced CO_2 Methanation Activity of Ni/Anatase Catalyst by Tuning Strong Metal − Support Interactions, ACS Catal. 9 (2019) 6342-6348.

[51] V. Nichele, M. Signoretto, F. Menegazzo, I. Rossetti, G. Cruciani, Hydrogen production by ethanol steam reforming: Effect of the Synthesis Parameters on the Activity of Ni/TiO_2 Catalysts, Int. J. Hydrogen Energ., 39 (2014) 4252-4258.

[52] I. Rossetti, J. Lasso, E. Finocchio, G. Ramis, V. Nichele, M. Signoretto, A. Di Michele, TiO_2-Supported Catalysts for the Steam Reforming of Ethanol, Appl. Catal. A, 477 (2014) 42-53.

[53] X. Li, J. Lin, L. Li, Y. Huang, X. Pan, S. E. Collins, Y. Ren, Y. Su, L.i Kang, X. Liu, Y. Zhou, H. Wang, A. Wang, B. Qiao, X. Wang, Tao Zhang, Controlling CO_2 Hydrogenation Selectivity by Metal-Supported Electron Transfer, Angew. Chem. Int. Ed. 59 (2020) 19983-19989.

[54] C. Rivera-Cárcamo, C. Scarfiello, A. B. García, Y. Tison, H. Martinez, W. Baaziz, O. Ersen, C. Le Berre, P. Serp, Stabilization of Metal Single Atoms on Carbon and TiO_2 Supports for CO_2 Hydrogenation: The Importance of Regulating Charge Transfer, Adv. Mater. Interfaces, (2020) doi.org/10.1002/admi.202001777.

[55] M. J. Jackman, A. G. Thomas, C. Muryn, Photoelectron Spectroscopy Study of Stoichiometric and Reduced Anatase TiO_2(101) Surfaces: The Effect of Subsurface Defects on Water Adsorption at Near-Ambient Pressures, J. Phys. Chem. C, 119 (2015) 13682-13690.

[56] I. Ro, J. Resasco, P. Christopher, Approaches for Understanding and Controlling Interfacial Effects in Oxide-Supported Metal Catalysts, ACS Catal., 8 (2018) 7368-7387.

[57] B. Yan, B. Zhao, S. Kattel, Q. Wu, S. Yao, D. Su, J. G. Chen, Tuning CO_2 Hydrogenation Selectivity via Metal-Oxide Interfacial Sites, J. Catal. 374 (2019) 60-71.

[58] S. Kattel, P. Liu, J. G. Chen, Tuning Selectivity of CO_2 Hydrogenation Reactions at the Metal/Oxide Interface, J. Am. Chem. Soc., 139 (2017) 9739-9754.

[59] C. Vogt, E. Groeneveld, G. Kamsma, M. Nachtegaal, L. Lu, C. J. Kiely, P. H. Berben, F. Meirer, B. M. Weckhuysen, Unravelling Structure Sensitivity in CO_2 Hydrogenation over Nickel, Nat. Catal., 1 (2018) 127-134.

[60] M.-M. Millet, G. Algara-Siller, S. Wrabetz, A. Mazheika, F. Girgsdies, D. Teschner, F. Seitz, A. Tarasov, S. V. Levchenko, R. Schlögl, E. Frei, Ni Single Atom Catalysts for CO_2 Activation, J. Am. Chem. Soc., 141 (2019)) 2451-2461.

[61] C. Mebrahtu, S. Perathoner, G. Giorgianni, S. Chen, G. Centi, F. Krebs, R. Palkovits, S. Abate, Deactivation Mechanism of Hydrotalcite-Derived Ni-AlO_x Catalysts during Low-Temperature CO_2 Methanation via Ni-Hydroxide Formation and the Role of Fe in Limiting this Effect, Catal. Sci. Technol., 9 (2019) 4023-4035.

[62] A. Kokka, T. Ramantani, A. Petala, P. Panagiotopoulou, Effect of the Nature of the Support, Operating and Pretreatment Conditions on the Catalytic Performance of

Supported Ni Catalysts for the Selective Methanation of CO, Catal. Today, (2019) doi:https://doi.org/10.1016/j.cattod.2019.04.015.

[63] A. Karelovic, P. Ruiz, Mechanistic Study of Low Temperature CO_2 Methanation over Rh/TiO_2 Catalysts, J. Catal., 301 (2013) 141-153.

[64] X. Wang, Y. Hong, H.Shi, J. Szanyi, Kinetic Modeling and Transient DRIFTS–MS Studies of CO_2 Methanation over Ru/Al_2O_3 catalysts, J. Catal. 343 (2016) 185-195.

[65] R. A. Hubble, J. Y. Lim, J. S. Dennis, Kinetic Studies of CO_2 Methanation over a $Ni/g\text{-}Al_2O_3$ Catalyst, Faraday Discuss., 192 (2016) 529-544.

[66] A. Westermann, B. Azambre, M.C. Bacariza, I. Graça, M.F. Ribeiro, J.M. Lopes, C. Henriques, Insight into CO_2 Methanation Mechanism over NiUSY Zeolites: An Operando IR Study, Appl. Catal. B, 174-175 (2015) 120-125.

[67] E. Baumgarten, G. Meyer, Hydrogen Spillover Through the Gas Phase. Some Kinetic Aspects. React. Kinet., Catal. Lett., 71 (2000) 325-333.

[68] E.; Baumgarten, R. Krupp, Hydrogenation of Hexene1 by Gas Phase Spillover Hydrogen. Influence of Substances Added in the Reaction Chamber, Without Contact to the Catalyst, React. Kinet. Catal. Lett., 70 (2000) 35-41.

[69] R. Prins, Hydrogen Spillover. Facts and Fiction, Chem. Rev., 112 (2012) 2714-2738.

[70] A. Karelovic, P. Ruiz, Improving the Hydrogenation Function of $Pd/\gamma\text{-}Al_2O_3$ Catalyst by $Rh/\gamma\text{-}Al_2O_3$ Addition in CO_2 Methanation at Low Temperature, ACS Catal., 3 (2013) 2799-2812.

[71] C. Swalusa, M. Jacquemin, C. Poleunis, P. Bertrand, P. Ruiz CO_2 Methanation on $Rh/\gamma\text{-}Al_2O_3$ Catalyst at Low Temperature: “In Situ” Supply of Hydrogen by Ni/Activated Carbon Catalyst, Appl. Catal. B, 125 (2012) 41-50.

[72] T. Inui, Highly Effective Conversion of Carbon Dioxide to Valuable Compounds on Composite Catalysts, Catal. Today, 29 (1996) 329-337.

[73] S. K. Beaumont, S. Alayoglu, C. Specht, N. Kruse, G. A. Somorjai, Nanoscale Demonstration of Hydrogen Atom Spillover and Surface Diffusion Across Silica Using the Kinetics of CO_2 Methanation Catalyzed on Spatially Separate Pt and Co Nanoparticles, Nano Lett., 14 (2014) 4792-4796.

[74] S. K. Beaumont, S. Alayoglu, C. Specht, W. D. Michalak, V. V. Pushkarev, J. Guo, N. Kruse, G. A. Somorjai, Combining in Situ NEXAFS Spectroscopy and CO_2 Methanation Kinetics To Study Pt and Co Nanoparticle Catalysts Reveals Key Insights into the Role of Platinum in Promoted Cobalt Catalysis, J. Am. Chem. Soc., 136 (2014) 9898-9901.

[75] Z Yan, Q. Liu, L. Liang, J. Ouyang, Surface hydroxyls mediated CO_2 methanation at ambient pressure over attapulgite-loaded Ni-TiO_2 composite catalysts with high activity and reuse ability, J. CO_2 Utilization, 47 (2021) 101489.

[76] Y. Guo, S. Mei, K. Yuan, D.-J. Wang, H.-C. Liu, C.-H. Yan, Y.-W. Zhang, Low-Temperature CO_2 Methanation over CeO_2-Supported Ru Single Atoms, Nanoclusters, and Nanoparticles Competitively Tuned by Strong Metal−Support Interactions and H-Spillover Effect, ACS Catal., 8 (2018) 6203-6215.

[77] J. Huang, X. Li, X. Wang, X. Fang, H. Wang, X. Xu, New Insights into CO_2 Methanation Mechanisms on Ni/MgO Catalysts by DFT Calculations: Elucidating Ni and MgO Roles and Support Effects, J. CO_2 Util., 33 (2019) 55-63.

[78] G Hu, Z. Wu, D.-e. Jiang, First Principles Insight into H_2 Activation and Hydride Species on TiO_2 Surfaces, J. Phys. Chem. C, 122 (2018) 20323-20328.

[79] R.n Wang, H. Fan, The mechanism of H_2 and H_2O desorption from bridging hydroxyls of a TiO_2(110) surface, Catal. Sci. Technol., 7 (2017) 251-264.

[80] W. Lin, H. Cheng, L. He, Y. Yu, F. Zhao, High Performance of Ir-Promoted Ni/TiO_2 Catalyst toward the Selective Hydrogenation of Cinnamaldehyde, J. Catal., 303 (2013) 110-116.

[81] P. Panagiotopoulou, D. I. Kondarides, Effects of Alkali Additives on the Physicochemical Characteristics and Chemisorptive Properties of Pt/TiO_2 Catalysts, J. Catal., 260 (2008) 141-149.

[82] P. Panagiotopoulou, D. I. Kondarides, Effects of Promotion of TiO_2 with Alkaline Earth Metals on the Chemisorptive Properties and Water–Gas Shift Activity of Supported Platinum Catalysts, App. Catal. B, 101 (2011) 738-746.

[83] Z. He, M. Hu, X. Wang, Highly Effective Hydrodeoxygenation of Guaiacol on Pt/TiO_2: Promoter Effects, Catal. Today, 302 (2018) 136-145.

[84] X.-L. Yin, M. Calatayud, H. Qiu, Y. Wang, A. Birkner, C. Minot, C. Wöll, Diffusion versus Desorption: Complex Behavior of H Atoms on an Oxide Surface, ChemPhysChem, 9 (2008) 253-256.

[85] M. M. Islam, M. Calatayud, G. Pacchioni, Hydrogen Adsorption and Diffusion on the Anatase TiO_2(101) Surface: A First-Principles Investigation, J. Phys. Chem. C, 115 (2011) 6809.

[86] S.-C. Li, Z. Zhang, D. Sheppard, B. D. Kay, J. M. White, Y. Du, I. Lyubinetsky, G. Henkelman, Z. Dohnálek, Intrinsic Diffusion of Hydrogen on Rutile TiO_2(110), J. Am. Chem. Soc., 130 (2008) 9080-9088.

[87] K. Liu, P. Yan, H. Jiang, Z. Xia, Z. Xu, S. Bai, Z. C. Zhang, Silver Initiated Hydrogen Spillover on Anatase TiO_2 Creates Active Sites for Selective Hydrodeoxygenation of Guaiacol, J. Catal., 369 (2019) 396-404.

[88] C.g Mao, J. Wang, Y. Zou, G. Qi, J. Yi, Y. Loh, T. Zhang, M. Xia, J. Xu, F. Deng, M. Ghoussoub, N. P. Kherani, L. Wang, H. Shang, M. Li, J. Li, X. Liu, Z. Ai, G. A. Ozin, J. Zhao, L. Zhang, J. Am. Chem. Soc., 142 (2020), 17403-17412.

[89] E. Baumgarten, R. Krupp, Gas Phase Hydrogen Spillover and Oxygen Content, React. Kinet. Catal. Lett., 70 (2000) 27-33.

[90] I. A. Razzhivina, G. A. Badun, M. G. Chernysheva, A. V. Garshev, V. P. Shevchenko, K. V. Shevchenko, I. Y. Nagaev, N. E. Shchepina, Hydrogen Spillover through a Gas Phase, Mendeleev Commun, 26 (2016) 59-60.

[91] E. Baumgarten, L. Maschke, Hydrogen Spillover through the Gas Phase: Reaction with Graphite and Activated Carbon, Appl. Catal. A, 202 (2000) 171-177.

[92] M. S. Spencer, R. Burch, S. E. Golunski, Comments on “Hydrogen Spillover through Gas Phase Transport of Hydrogen Atoms”, J. Catal., 126 (1990) 311-313.

[93] S. S. Han, H. Kim, N. Park, Effect of Shuttling Catalyst on the Migration of Hydrogen Adatoms: A Strategy for the Facile Hydrogenation of Graphene, J. Phys. Chem. C, 115 (2011) 24696-24701.

[94] Y. Zhu, D. Liu, M. Meng, H_2 Spillover Enhanced Hydrogenation Capability of TiO_2 Used for Photocatalytic Splitting of Water: a Traditional Phenomenon for New Applications, Chem. Commun., 50 (2014) 6049-6051.

[95] D. Panayotov, E. Ivanova, M. Mihaylov, K. Chakarova, T. Spassov, K. Hadjiivanov, Hydrogen Spillover on Rh/TiO_2: the FTIR Study of Donated Electrons, co-Adsorbed CO and H/D Exchange, Phys. Chem. Chem. Phys., 17 (2015) 20563-20573.

[96] W. Wan, X. Nie, M. J. Janik, C. Song, X. Guo, Adsorption, Dissociation, and Spillover of Hydrogen over Au/TiO_2 Catalysts: The Effects of Cluster Size and Metal−Support Interaction from DFT, J. Phys. Chem. C, 122 (2018) 17895-17916.

[97] E. S. Putna, R. J. Gorte, J. M. Vohs, G. W. Grahamy, Evidence for Enhanced Dissociation of CO on Rh/Ceria, J. Catal., 178 (1998) 598-603.

[98] R. Burch, A. R. Flambard, Strong Metal-Support Interactions in Nickel-Titania Catalysts: The Importance of Interfacial Phenomena, J. Catal., 78 (1982) 389-405.

[99] X. Jia, X. Zhang, N. Rui, X. Hu, C.-j. Liu, Structural Effect of Ni/ZrO_2 Catalyst on CO_2 Methanation with Enhanced Activity, Appl. Catal. B, 244 (2019) 159-169.

[100] S. D. Senanayake, P. J. Ramírez, I. Waluyo, S. Kundu, K. Mudiyanselage, Z. Liu, Z. Liu, S. Axnanda, D. J. Stacchiola, J. Evans, J. A. Rodriguez, Hydrogenation of CO_2 to Methanol on CeOx/Cu(111) and ZnO/Cu(111) Catalysts: Role of the Metal–Oxide Interface and Importance of Ce^{3+} Sites, J. Phys. Chem. C, 120 (2016) 1778-1784.

[101] Sh. Lin, Z. Hao, J. Shen, X. Chang, S. Huang, M. Li, X. Ma, Enhancing the CO_2 methanation activity of Ni/CeO_2 via activation treatment-determined metal-support interaction, J. Energy Chem. 59 (2021) 334-342.

[102] W. Li, H. Wang, X. Jiang, J. Zhu, Z. Liu, X. Guo, C. Song, A short review of recent advances in CO_2 hydrogenation to hydrocarbons over heterogeneous catalysts, RSC Adv., 8 (2018) 7651-7669.

[103] Y. Hinuma, T. Toyao, T. Kamachi, Z. Maeno, S. Takakusagi, S. Furukawa, I. Takigawa, K.-i. Shimizu, Density functional theory calculations of oxygen vacancy formation and subsequent molecular adsorption on oxide surfaces, J. Phys. Chem. C, 122 (2018) 29435-29444.

[104] J. Kapicka, N. I. Jaeger, G. Schulz-Ekloff, Evidence for a hydrogen spillover effect in the deposition of coke on a nickel-faujasite catalyst during syngas conversion, Appl. Catal. A: General, 84 (1992) 47-55.

[105] C.-j. Liu, J. Ye, J. Jiang, Y. Pan, Progresses in the preparation of coke resistant Ni-based catalyst for steam and CO_2 reforming of methane, ChemCatChem, 3 (2011) 529-541.

[106] G. E. Batley, A. Ekstrom, D. A. Johnson, Studies of topochemical heterogeneous catalysis: 3. Catalysis of the reduction of metal oxides by hydrogen, J. Catal, 34 (1974) 368-375.

[107] L. Shen, J. Xu, M. Zhu, Y.-F. Han, Essential Role of the Support for Nickel-Based CO_2 Methanation Catalysts, ACS Catal., 10 (2020) 14581−14591.

[108] I. T. Chashechnikova, V. M. Vorotyntsev, A. V. Gette, G. I. Golodets, Effect of Rutile/Anatase Ratio on Catalytic Properties of Co−TiO_2 Catalysts for Fischer-Tropsch Synthesis, React. Kinet. Catal. Lett., 40 (1989) 47-51.

[109] K. Shimura, T. Miyazawa, T. Hanaoka, S. Hirata Fischer–Tropsch Synthesis over TiO_2 Supported Cobalt Catalyst: Effect of TiO_2 Crystal Phase and Metal Ion Loading, Appl. Catal. A, 460-461 (2013) 8-14.